Title.

A disrupted compartment boundary underlies abnormal cardiac patterning and congenital heart defects

Author List.

Irfan S. Kathiriya[1,#], Martin H. Dominguez[2,3,14], Kavitha S. Rao[1,2], Jonathon M. Muncie-Vasic[2], W. Patrick Devine[2,15], Kevin M. Hu[1,2,16], Swetansu K. Hota[2,17], Bayardo I. Garay[1,18], Diego Quintero[2,19], Piyush Goyal[1,2,20], Megan N. Matthews[1, 21], Reuben Thomas[2], Tatyana Sukonnik[2,22], Dario Miguel-Perez[2], Sarah Winchester[2], Emily F. Brower[2], André Forjaz[4], Pei-Hsun Wu[4], Denis Wirtz[4], Ashley L. Kiemen[4,5,6,7,8], Benoit G. Bruneau[2,9,10,11,12,13,#]

[#]These authors jointly supervised this work.

Correspondence to I.S.K. (irfan.kathriya@ucsf.edu) and B.G.B. (benoit.bruneau@gladstone.ucsf.edu)

Affiliations.

[1] Department of Anesthesia and Perioperative Care, University of California, San Francisco, San Francisco, CA

[2] Gladstone Institutes, San Francisco, CA

[3] Department of Medicine, University of California, San Francisco, San Francisco, CA

[4] Department of Chemical and Biomolecular Engineering, Johns Hopkins University, Baltimore, MD

[5] Sol Goldman Pancreatic Cancer Research Center, Department of Pathology, Johns Hopkins University

[6] Department of Chemical & Biomolecular Engineering, Johns Hopkins University

[7] Department of Oncology, Johns Hopkins University

[8] Department of Functional Anatomy and Evolution, Johns Hopkins University

[9] Roddenberry Center for Stem Cell Biology and Medicine, Gladstone Institutes, San Francisco, CA

[10] Department of Pediatrics, University of California, San Francisco, San Francisco, CA

[11] Cardiovascular Research Institute, University of California, San Francisco, San Francisco, CA

[12] Institute for Human Genetics, University of California; San Francisco, CA, USA.

[13] The Eli and Edythe Broad Center for Regeneration Medicine and Stem Cell Research, University of California; San Francisco, CA, USA.

[14] Current address: Department of Medicine, Drexel College of Medicine, Philadelphia PA

[15] Current address: Department of Pathology, University of California, San Francisco, San Francisco, CA

[16] Current address: Creighton University School of Medicine, Omaha, NE

[17] Current address: Herman B. Wells Center for Pediatric Research, Indiana University School of Medicine, Indianapolis, IN

[18] Current address: Department of Anesthesiology, Washington University in St. Louis, St. Louis, MO

[19] Current address: Department of Human Genetics, Emory University School of Medicine, Atlanta, GA

[20] Current address: Department of Interventional Radiology, University of Utah School of Medicine, Salt Lake City, UT

[21] Current address: California Institute of Technology, Pasadena, CA

[22] Deceased

Abstract.

Failure of septation of the interventricular septum (IVS) is the most common congenital heart defect (CHD), but mechanisms for patterning the IVS are largely unknown. Here, we show that a *Tbx5*$^{+}$/*Mef2cAHF*$^{+}$ progenitor lineage forms a compartment boundary bisecting the IVS. This coordinated population originates at a first- and second heart field interface. Ablation of *Tbx5*$^{+}$/*Mef2cAHF*$^{+}$ progenitors cause IVS disorganization, right ventricular hypoplasia and mixing of IVS lineages. Reduced dosage of the CHD transcription factor TBX5 disrupts boundary position and integrity, resulting in ventricular septation defects (VSDs) and patterning defects, including misexpression of *Slit2* and *Ntn1*, which encode guidance cues. Reducing NTN1 dosage partly rescues cardiac defects in *Tbx5* mutant embryos. Loss of *Slit2* or *Ntn1* causes VSDs and perturbed septal lineage distributions. Thus, we identify *Tbx5* as a candidate selector gene, directing progenitors and regulating essential cues, to pattern a compartment boundary for proper cardiac septation, revealing mechanisms for cardiac birth defects.

Main text.

Organogenesis relies on fine tissue patterning, and disturbances cause organ malformations that result in birth defects. Examples of prevalent birth defects resulting from abnormal patterning include congenital limb abnormalities, neural tube defects or congenital heart defects (CHDs).

CHDs are the most common birth defects and are a leading cause of morbidity and mortality in childhood [1]. CHDs are thought to result from alterations to the orchestrated patterning of heart development. Nearly half of all patients with CHDs have atrial septal defects (ASDs) or ventricular septal defects (VSDs), which is an abnormality of the formation of the interventricular septum (IVS) [2,3]. Septal defects can occur either in isolation or combined with other anatomic defects, including abnormal chamber formation. For example, atrioventricular (AV) canal defects

include VSDs, ASDs and abnormal development of the AV valves, with severe cases leading to chamber hypoplasia and functional single ventricle physiology [4]. There is a large gap in our understanding of how early developmental events pattern cardiac morphogenesis and anatomy. Addressing this understudied need can inform diagnostic prognosis, family planning and therapeutic approaches for CHDs.

Complete atrioventricular septation into four chambers allows for separation of systemic and pulmonary circulations, and enables higher levels of oxygen for transport in arterial blood. Although formation of the IVS, which separates the left ventricle (LV) and right ventricle (RV), is an intricate and poorly understood process, some progress has been made to determine the embryonic origins of the IVS. Dye-labeling studies in chick have shown that the IVS is derived from the bulbo-ventricular region between the future RV and LV [5], and both the RV and LV supply compact layer cells and some lateral trabecular cells to form the core of the IVS [6–8]. Likewise, discovery of the *Ganglion Nodosum* epitope from chick, which demarcates the primary interventricular foramen and subsequently the IVS, AV junction and ventricular conduction system in mouse, chick and humans, has led to the description of a “primary ring” for the ventricular septum [9–11]. Consistent with the “primary ring”, cell behaviour of IVS primordia displays circumferential oriented cell growth from the interventricular groove at the outer curvature to the inner curvature at E10.5 [12]. In addition, some gene expression domains are enriched in the IVS. For example, *Tbx5* is expressed in the LV and IVS, and proper TBX5 dosage is essential for IVS formation [13]. *Irx2* is expressed in the IVS and adjacent ventricular tissue [14], and *Lyz2* is expressed at the bulbo-ventricular groove at E9.5 at the site of the future IVS [15]. Further, the *Lyz2*$^{+}$ lineage contributes cells to the muscular portion throughout the developing IVS [15]. This evidence delineates the embryonic origins of the IVS as a distinct region of the developing heart, although its earliest progenitors and regulation are unclear.

100 Studies have suggested that the linear heart tube is organized into specific segments [16,17],
101 including the IVS [5,18]. It is increasingly apparent in the developing mouse heart that discrete early
102 cardiac progenitors in mesoderm are already fated to contribute to regionalization of specific
103 cardiac anatomy [19–26]. The first heart field (FHF) gives rise primarily to the left ventricle (LV) and
104 parts of the atria, while the second heart field (SHF) contributes predominantly to the right ventricle
105 (RV), outflow tract (OFT) and portions of the atria [21]. The heart fields can be largely recapitulated
106 by marking lineage-labelled progenitors at gastrulation [24,25]. Specifically, a cell lineage labelled by
107 the CHD-linked transcription factor *Tbx5* (*Tbx5*$^{+}$ lineage) contributes to the LV, IVS and atria,
108 while the anterior heart field enhancer of *Mef2c* (*Mef2cAHF*$^{+}$) lineage largely contributes to the
109 RV, IVS and OFT [25].

110 An aspect of proper tissue patterning entails the establishment of compartment
111 boundaries to separate neighboring fields of cells that exhibit discrete functions [27–29]. Few
112 compartment boundaries have been identified in mammals, notably the dorso-ventral patterning
113 of the limb [30–32] and the midbrain-hindbrain boundary [33]. In the developing mouse heart,
114 retrospective clonal cell analysis shows segregation of LV- and RV-lineages on either the left or
115 right side of the IVS, establishing a presumptive mutual border between the two non-intermingling
116 compartments [12,25,34], reminiscent of a compartment boundary[10–12]. Moreover, this evidence has
117 led to a prediction of a compartment boundary at the IVS that acts as a barrier to cell mixing
118 between the LV and RV [12,25,34]. Using an intersectional-lineage labelling approach, a subset of
119 cardiac progenitor cells labeled by both *Tbx5*$^{+}$/*Mef2cAHF*$^{+}$ were described with contributions to
120 the left side of the IVS, delineating a cell lineage of an apparent compartment boundary [25].
121 Understanding the roles of a *Tbx5*$^{+}$/*Mef2cAHF*$^{+}$ lineage-labeled compartment boundary at the IVS
122 may reveal clues about IVS patterning with potential relevance for VSD etiologies. More broadly,
123 how disturbances to compartment boundaries contribute to birth defects is largely unknown.

124 Here, we combined genetic lineage labeling with lightsheet microscopy to follow
125 contributions of *Tbx5*$^{+}$*/Mef2cAHF*$^{+}$ precursors to a compartment boundary during cardiac
126 morphogenesis. We ablated *Tbx5*$^{+}$*/Mef2cAHF*$^{+}$ precursors to determine the essential roles of the
127 lineage-labeled compartment boundary for cardiac septation and chamber development. By
128 leveraging a genetic lesion of the CHD gene *Tbx5,* our work uncovers the genetic regulation of
129 the *Tbx5*$^{+}$*/Mef2cAHF*$^{+}$ lineage-labeled compartment boundary for proper IVS patterning. We
130 deployed single cell RNA sequencing (scRNA-seq) to discover TBX5-sensitive cues that are
131 essential for compartment boundary regulation and formation of the IVS during heart
132 development.
133
134 Early cardiac progenitors for the IVS, IAS and AV complex regions. We used conditional dual
135 lineage labelling by *Tbx5*$^{CreERT2/+}$ or *Mef2cAHF-DreERT2* and marked cells during gastrulation at
136 embryonic day (E) 6.5 by a single dose of tamoxifen-induced recombination. We followed
137 separate reporter-labeled lineages by epifluorescence microscopy, histology or lightsheet
138 microscopy (Fig. 1a-f). At E14.5, the *Tbx5*$^{+}$ lineage contributed to the left side of the IVS, often
139 ending at a presumptive line marked at the apex by the interventricular (IV) groove, consistent
140 with previous reports suggesting a lineage boundary [12,25,34]. *Tbx5*$^{+}$ and *Mef2cAHF*$^{+}$ lineages
141 showed largely complementary patterns, with notable overlap of *Tbx5*$^{+}$ and *Mef2cAHF*$^{+}$ lineages
142 at the IVS, AV complex region, and inter-atrial septum (IAS) (Fig. 1b, d, f).
143 To better visualize the *Tbx5*$^{+}$*/Mef2cAHF*$^{+}$ lineage, we used a conditional intersectional-
144 lineage labeling approach. Using a lineage reporter that is responsive to both CreERT2 and
145 DreERT2 [35], we observed a spatial pattern of the *Tbx5*$^{+}$*/Mef2cAHF*$^{+}$ lineage in the IVS, AV
146 complex region, and IAS (Fig. 1g). At E14.5, the septal lineage extended to the apex of the heart
147 via the IVS, to the base of the heart at the AV complex region, as well as to the IAS superiorly[15–
148 18] (Fig. 1h-j). These results expanded upon previous findings in the developing IVS at E10.5 [25],

149 by identifying contributions from *Tbx5*$^{+}$/*Mef2cAHF*$^{+}$ progenitors to additional anatomic sites during
150 chamber formation and septation. Moreover, lineage contributions to sites of chamber septation
151 were derived from *Tbx5*$^{+}$/*Mef2cAHF*$^{+}$ progenitors at E6.5 (Extended Data Fig. 1a-c), but not later
152 at E8.5 or E10.5, implicating a narrow, early window for capturing *Tbx5*$^{+}$/*Mef2cAHF*$^{+}$ septal
153 progenitors during cardiac mesoderm formation.
154
155 <u>*Tbx5*$^{+}$/*Mef2cAHF*$^{+}$ septal lineage is prefigured in early mouse heart development.</u> To characterize
156 the lineage derived from *Tbx5*$^{+}$/*Mef2cAHF*$^{+}$ septal progenitors during early heart development, we
157 examined the localization of the lineage prior to heart tube formation at E8.0 (Extended Data Fig.
158 1d-f, Fig. 2, Video 1). By lightsheet imaging, the pattern of the *Tbx5*$^{+}$/*Mef2cAHF*$^{+}$ lineage was
159 detected at the dorsal aspect of the *Tbx5*$^{+}$ lineage, at an interface between *Tbx5*$^{+}$ and *Tbx5*$^{-}$
160 lineage compartments (Fig. 2a-e"). Cell segmentation at this early stage revealed that the
161 *Tbx5*$^{+}$/*Mef2cAHF*$^{+}$ lineage resembled a nascent halo of cells that became readily apparent at later
162 stages of heart development (Fig. 2f-i).
163 We further examined the lineage contributions of *Tbx5*$^{+}$/*Mef2cAHF*$^{+}$ septal progenitors at
164 subsequent timepoints during cardiac morphogenesis. At the linear heart tube stage at E8.25, the
165 labeled *Tbx5*$^{+}$/*Mef2cAHF*$^{+}$ lineage appeared intricately arranged into a ring of cells between the
166 future left and right ventricles (Fig. 2j, k). This circlet configuration was maintained during
167 rightward looping of the heart at E8.5 (Fig. 2o-q) and subsequent chamber formation. At E10.5,
168 we observed a band of lineage-labeled cells from the IV groove at the outer curvature to the inner
169 curvature near the AV groove that extended posteriorly to the atria (Fig. 2r-t), reminiscent of the
170 "primary ring" [9–11] and consistent with oriented cell growth of the developing IVS [12]. Optical
171 sections showed the labeled lineage superiorly at a crossroads of the AV canal, outflow tract and
172 atria (Fig. 2s). This populates a morphogenetic nexus, where VSDs can occur due to abnormal
173 connections between the IVS and the AV canal, outflow tract cushions, or the muscular septum

174 itself. In the atria, we noted lineage-labeled cells at the midline, superiorly and inferiorly
175 (Supplemental Figure 1a-e), consistent with clonal growth in the body of the atria [12]. This suggests
176 that the *Tbx5*$^{+}$*/Mef2cAHF*$^{+}$ lineage potentially marks the presumptive location of the IAS for later
177 stages. Consequently, this data is consistent with a notion that the *Tbx5*$^{+}$*/Mef2cAHF*$^{+}$ lineage is
178 configured early in heart development, well before subsequent morphogenetic events of chamber
179 formation and cardiac septation.
180
181 IVS disorganization and ventricular hypoplasia from cell ablation of *Tbx5*$^{+}$/*Mef2cAHF*$^{+}$
182 progenitors. To determine a role for the *Tbx5*$^{+}$*/Mef2cAHF*$^{+}$ septal progenitors during heart
183 development, we conditionally ablated these cells at E6.5. To this end, we generated an
184 intersectional recombinase-responsive *DTA176* knock-in mouse allele at the *Hip11* safe-harbor
185 locus, by which cells would be killed where approximately 100-200 molecules of DTA176 were
186 expressed [36,37]. Upon a single dose of tamoxifen administration to pregnant dams at E6.5,
187 intersectional-*DTA* mutant (*Tbx5*$^{CreERT2/+}$*; Mef2cAHF-DreERT2; Hip11*$^{Intersectional\text{-}DTA176/+}$) embryos
188 displayed RV hypoplasia (i.e. a reduction in RV chamber size) at E9.5 (Fig. 3a, b) and E12.5 (Fig.
189 3c-j), together with IVS disorganization and non-compaction with a blunted IV groove (Fig. 3h, j).
190 Further, there were defects of the AV complex region and absence of the IAS (Fig. 3h, j). A few
191 *Tbx5*$^{+}$*/Mef2cAHF*$^{+}$ lineage cells remained in mutant embryos, likely reflecting some degree of
192 inefficient dual recombination of both the reporter allele [38,39] and the intersectional-*DTA* transgene
193 [40]. Beyond E12.5, intersectional-*DTA* mutant embryos were not recovered. Results of
194 *Tbx5*$^{+}$/*Mef2cAHF*$^{+}$ progenitor ablation contrasted with findings after the ablation of the LV-
195 enriched *Hand1*$^{+}$ lineage, which caused LV hypoplasia at E10.5 and full recovery of the LV by
196 E16.5 [41]. Hence, our findings suggested that the *Tbx5*$^{+}$*/Mef2cAHF*$^{+}$ septal progenitors were not
197 only important for IVS development and AV septation, but also for RV chamber formation.
198

199 Lineage mixing from disruption of an IVS compartment boundary upon ablation of
200 *Tbx5*$^{+}$*/Mef2cAHF*$^{+}$ septal progenitors. We hypothesized that the *Tbx5*$^{+}$*/Mef2cAHF*$^{+}$ septal
201 progenitors establish a compartment boundary at the IVS. Upon ablation of *Tbx5*$^{+}$*/Mef2cAHF*$^{+}$
202 septal progenitors, we predicted that if either lineage expanded into the other ventricular chamber,
203 then this would suggest lineage mixing from loss of compartment boundary integrity. To determine
204 if *Tbx5*$^{+}$*/Mef2cAHF*$^{+}$ septal progenitors were essential for a compartment boundary at the IVS, we
205 tested the effects of ablating *Tbx5*$^{+}$*/Mef2cAHF*$^{+}$ septal progenitors on lineage segregation (Fig.
206 3k-n'). We quantified the distribution of the *Mef2cAHF*$^{+}$ or *Tbx5*$^{+}$ lineages at E10.5 after a single
207 dose of tamoxifen administration at E6.5 using two metrics. First, we assessed each fluorescently-
208 labeled lineage by distribution in the RV or LV. We observed that cells of the *Mef2cAHF*$^{+}$ lineage
209 were enriched in the RV of control embryos (*Tbx5*$^{CreERT2/+}$*;Mef2cAHF-DreERT2;Hip11*$^{+/+}$), and this
210 distribution was not different in mutant intersectional-*DTA* embryos (*Tbx5*$^{CreERT2/+}$*;Mef2cAHF-*
211 *DreERT2;Hip11*$^{Intersectional\text{-}DTA176/+}$) (Extended Data Fig. 2a-c). Cells of the *Tbx5*$^{+}$ lineage were
212 normally enriched in the LV and nearly absent in the RV of controls. However, in mutant
213 intersectional-*DTA* embryos, a larger percentage of *Tbx5*$^{+}$ lineage cells were located in the RV
214 (Fig 3o).

215 Second, we quantified the fluorescence intensity as a linear profile across the ventricular
216 chambers by lightsheet microscopy (Fig. 3p). Cells of the *Mef2cAHF*$^{+}$ lineage were again enriched
217 in the RV in controls, and showed reduced fluorescence in the LV in mutant intersectional-*DTA*
218 embryos (Extended Data Fig. 2d-f). Moreover, cells of the *Tbx5*$^{+}$ lineage were again highly
219 enriched in the LV and rarely found in the RV. In contrast, cells of the *Tbx5*$^{+}$ lineage in
220 intersectional-*DTA* mutants were observed more rightward, including in the RV (Fig 3q, r).
221 Therefore, we inferred that *Tbx5*$^{+}$*/Mef2cAHF*$^{+}$ progenitors were essential for preventing lineage
222 mixing between the RV and LV, by maintaining compartment boundary integrity at the developing

223 IVS. This data may imply preferential regulation of first heart field derivatives over the adjacent
224 second heart field derivatives.
225
226 Heterozygous loss of *Tbx5* in the IVS leads to VSDs. *TBX5* is a transcription factor gene that
227 causes VSDs in Holt-Oram Syndrome from haploinsufficiency in humans [42–44] and mice [45]. We
228 wondered if heterozygous loss of *Tbx5* in the IVS would cause VSDs. We used the *Mef2cAHF-*
229 *Cre* [46] in combination with a conditional deletion of *Tbx5* (*Tbx5*^{flox}) [45], to conditionally delete *Tbx5*
230 heterozygously in a domain that overlaps with *Tbx5* expression at the IVS [13]. We observed
231 membranous VSDs in *Mef2cAHF-Cre*;*ROSA26*$^{mTmG/+}$;*Tbx5*$^{flox/+}$ mutant embryos (n=4/7)
232 compared to controls (n=0/3), at E14.5 (Extended Data Fig. 3a-c). This provided evidence that
233 appropriate *Tbx5* dosage in the IVS was essential for proper ventricular septation. Whether *Tbx5*
234 is required in *Mef2cAHF*$^{+}$ progenitors or in a subsequent stage for IVS formation remains to be
235 determined.
236
237 Disturbed septal lineage contributions from reduced *Tbx5.* As TBX5 dosage reduction globally or
238 only in the IVS results in VSDs, we reasoned that reducing TBX5 dosage may affect the regulation
239 of the *Tbx5*$^{+}$/*Mef2cAHF*$^{+}$ septal progenitors and their subsequent lineage contributions. We
240 evaluated a reduction of *Tbx5* using a hypomorphic (*Tbx5*^{CreERT2}) allele [44], which has been used
241 thus far in this study to follow the *Tbx5*$^{+}$ and *Tbx5*$^{+}$/*Mef2cAHF*$^{+}$ lineages, in combination with a
242 conditional deletion of *Tbx5* (*Tbx5*^{flox}) [45] at E6.5. This resulted in levels of *Tbx5* that are estimated
243 to be about 25% of wildtype in the *Tbx5*$^{+}$ lineage of *Tbx5* mutants. In control embryos
244 (*Tbx5*$^{CreERT2/+}$;*Mef2cAHF-DreERT2;ROSA26*$^{Ai66/Ai6}$), the *Tbx5*$^{+}$/*Mef2cAHF*$^{+}$ septal lineage
245 overlapped at the lineage front of the *Tbx5*$^{+}$ lineage in the IVS, from the base to the apex of the
246 heart at the IV groove, spanning from anterior to posterior of the heart in the IVS (Figure 4a-a",
247 Extended Data Fig. 4a, b, Video 2). Among *Tbx5*$^{CreERT2/flox}$ mutant embryos

248 (*Tbx5*$^{CreERT2/flox}$*;Mef2cAHF-DreERT2;ROSA26*$^{Ai66/Ai6}$), we found that reduced TBX5 dosage at E6.5
249 caused a spectrum of defects, frequently including VSDs, ASDs or AV canal defects at E14.5
250 (Fig. 4b-d'), reminiscent of features of Holt-Oram Syndrome [42,43,47]. The normally organized
251 distribution of the tdTomato$^+$ cells was highly irregular in the *Tbx5*$^{CreERT2/flox}$ mutant hearts
252 regardless of VSDs (Extended Data Fig. 4a-h). tdTomato$^+$ cells were less apparent in the posterior
253 IVS (Fig. 4a', a", b', b", c', c", d') and IAS (Supplemental Figure 2), and tdTomato$^+$ cells were
254 nearly absent in a heart that displayed a severe AV canal defect and chamber hypoplasia (Fig.
255 4d, d', Extended Data Fig. 4g, h).

256 We used quantitative morphometry to assess the position and distribution of the
257 *Tbx5*$^+$*/Mef2cAHF*$^+$ septal lineage at the IVS. We tested this by quantifying linear profiles of the
258 labeled *Tbx5*$^+$*/Mef2cAHF*$^+$ septal lineage in the heart. We found that both distribution and position
259 of the *Tbx5*$^+$*/Mef2cAHF*$^+$ septal lineage was disturbed in *Tbx5*$^{CreERT2/flox}$ mutants (Fig. 4e-h,
260 Extended Data Fig. 4i-k), including an increase of tdTomato$^+$ cells leftward in the LV, suggesting
261 abnormal lineage position. As well, we observed a broader band of *Tbx5*$^+$*/Mef2cAHF*$^+$ septal
262 lineage cells (Fig. 4g, h), suggesting that proper TBX5 dosage maintains integrity of the
263 compartment boundary marked by the *Tbx5*$^+$*/Mef2cAHF*$^+$ lineage at the IVS. We also observed a
264 reduction, or sometimes absence, of the labeled septal lineage among AV complex region cells,
265 as well as remnant atrial septal tissue in *Tbx5*$^{CreERT2/flox}$ mutants (Fig. 4d, d').

266 We further observed that cells of the *Tbx5*$^+$*/Mef2cAHF*$^+$ lineage in the IVS were arranged
267 like a stack of coins, especially from the apex to the mid-septum (Fig. 4a"). We wondered if proper
268 TBX5 dosage might be necessary for maintaining appropriate cell arrangement in the IVS.
269 Therefore, cell alignment was determined and quantified by two metrics, average orientation
270 score or directional coherency. In *Tbx5*$^{CreERT2/flox}$ mutant hearts, *Tbx5*$^+$*/Mef2cAHF*$^+$ lineage
271 (tdTomato$^+$) and *Tbx5*$^+$ lineage (ZsGreen$^+$) cells were reduced in the dominant direction of cell
272 orientation and were more frequently in the orientation orthogonal to the dominant direction (Fig.

273 4i-t, Extended Data Fig. 4l-s). Further, both lineages demonstrated worse directional coherency
274 in *Tbx5*$^{CreERT2/flox}$ mutants (Fig. 4t, Extended Data Fig. 4u). In a complementary analysis, we also
275 evaluated cell geometry and tissue architecture of the IVS using staining for cell borders by wheat
276 germ agglutinin (WGA) and nuclei by DAPI. We found in IVS cardiomyocytes of *Tbx5* mutants
277 that cell diameter and area was enlarged (Fig. 4u-x, Supplemental Figure 3a-h'), while cell
278 eccentricity (a measure of a cell's elongation) and nuclei density was reduced (Fig. 4y, z). Taken
279 together, this evidence supports a notion that TBX5 is important for proper cell arrangement in
280 the IVS.
281
282 <u>*Tbx5*-sensitive genes encode guidance cues</u>. To find downstream effectors of Tbx5 that may
283 mediate the regulation of *Tbx5*$^{+}$/*Mef2cAHF*$^{+}$ lineage cells, we applied scRNA-seq at E13.5, prior
284 to completion of ventricular septation. We micro-dissected the RV, LV and IVS+AV complex
285 regions in controls and *Tbx5* mutants (*Tbx5*$^{CreERT2/flox}$*;Mef2cAHF-DreERT2;ROSA26*$^{Ai66/Ai6}$) (Fig.
286 5a). These samples were labeled at E6.5 for progenitors of the *Tbx5*$^{+}$/*Mef2cAHF*$^{+}$ lineage
287 (*tdTomato*$^{+}$) and *Tbx5*$^{+}$ lineage (*ZsGreen*$^{+}$). In samples from each cardiac tissue region, we
288 detected clusters enriched for *Tnnt2*$^{+}$ cardiomyocytes (CMs), *Postn*$^{+}$ fibroblasts, *Plvap*$^{+}$
289 endothelial cells, *Tbx18*$^{+}$/*Wt1*$^{+}$ epicardial cells, *Hba-x*$^{+}$ red blood cells, and *C1qb*$^{+}$ white blood cells
290 (Fig. 5b, Extended Data Fig. 5A-i).
291 In particular, *tdTomato*$^{+}$ cells were most abundant among clusters of *Tnnt2*$^{+}$
292 cardiomyocytes (CMs) of the IVS+AV complex regions (Fig. 5c). However, we were unable to
293 identify a gene expression signature that was unique to the *Tbx5*$^{+}$/*Mef2cAHF*$^{+}$ lineage, beyond
294 the lineage marker itself, at this stage. Likewise, *ZsGreen*$^{+}$ cells were also enriched among
295 clusters of *Tnnt2*$^{+}$ CMs in this region (Fig. 5d), indicative of the *Tbx5*$^{+}$ lineage contribution to CMs
296 in the region, as well as a site of conditional reduction of *Tbx5* among *Tbx5* mutants.

297 We then focused our analysis on a subset of *Tnnt2*$^{+}$ enriched clusters from IVS+AV
298 complex regions. We identified genotype-enriched clusters that were abundant with cells from
299 controls (Cluster 5) or *Tbx5* mutants (Cluster 10) (Fig. 5e, f). In the mutant-enriched cluster 10,
300 genes typically expressed in ventricular trabeculae were enriched (Fig. 5g, h). These included
301 natriuretic peptide *Nppa*, transcription factor *Cited1,* and bone morphogenetic protein *Bmp10*,
302 suggesting ectopic expression of these trabecular genes in the IVS of *Tbx5* mutants. Intriguingly,
303 guidance cues *Netrin1* (*Ntn1)* and *Slit2,* which are best known for axonal development or
304 vasculogenesis [48], were also dysregulated (Fig. 5g, h, Extended Data Fig. 5j,k, Supplemenatal
305 Figure 4a, b). Notably, *SLIT2* is implicated as a CHD-risk gene in mice and humans [49–52]. For
306 *NTN1*, it's link to human CHD requires further clarification, as a copy number variation by
307 intragenic deletion of *NTN1*, along with heterozygous loss of 22q11.21 and gain of the Y
308 chromosome, was associated with septal defects in a patient [53]. Control-enriched cluster 5
309 included genes expressed in the AV complex region, encoding the Wnt co-receptor *Rspo3*,
310 morphogen *Bmp2*, and transcription factors *Tbx2* and *Tbx3*, and *Cdh2*, which encodes N-
311 Cadherin, suggesting that these genes are reduced in *Tbx5* mutants (Fig. 5g, h). As well, the
312 SLIT-receptor *Robo1,* which is implicated in mouse and human VSDs [49,51,54], and Netrin-receptor
313 *Unc5b,* were also downregulated in *Tbx5* mutant cells (Fig. 5g, h).
314 We examined differential gene expression between controls or *Tbx5* mutants in *tdTomato*$^{+}$
315 (*Tbx5*$^{+}$*/Mef2cAHF*$^{+}$ septal lineage) or *ZsGreen*$^{+}$ (*Tbx5*$^{+}$ lineage) CMs. We found many
316 differentially expressed genes that overlapped among comparisons of *tdTomato*$^{+}$ or *ZsGreen*$^{+}$
317 clusters, including *Nppa*, *Cited1,* and *Slit2*, consistent with findings from cluster-to-cluster
318 comparisons (Extended Data Fig. 5j, k).
319 We used orthogonal assays to validate candidate TBX5-sensitive genes. By fluorescence
320 *in situ* hybridization in formalin fixed paraffin embedded (FFPE) sections, we observed a reduction
321 of gene expression of *Bmp2, Robo1 and Unc5b* in the AV complex region of mutant hearts when

322 compared to controls. (Extended Data Fig. 6a-f"). We found that the IVS-enriched gene *Irx2* was
323 reduced in the IVS of *Tbx5* mutants (Extended Data Fig 6g-h'). As well, we detected expansion
324 of *Nppa* and *Slit2* into the IVS and compact layer of *Tbx5* mutant hearts, both of which are
325 normally expressed only in the trabecular regions of both ventricles of control hearts (Fig. 5i-l').
326 Moreover, we discovered *Ntn1* expression enriched in LV trabecular CMs and in a gradient across
327 the control IVS (Fig. 5m, m', Extended Data Fig. 6m-m"), consistent with immunostaining of NTN1
328 in the heart at E14.5 (Extended Data Fig. 6o). However, in *Tbx5* mutants, the *Ntn1* gradient was
329 flattened and expanded in the IVS by reduced TBX5 dosage (Fig. 5n, n'). Interestingly, we
330 observed abnormal *Nppa*, *Slit2* and *Ntn1* in *Tbx5* mutants with or without VSDs, suggesting that
331 this dysregulated gene expression was not secondary to VSDs (Extended Data Fig. 6i-n").
332 Notably, earlier at E11.5, *Ntn1* was LV-enriched during normal ventricular septation and broadly
333 expanded into the RV of *Tbx5* mutants, while *Slit2* appeared unchanged in *Tbx5* mutants
334 (Extended Data Fig. 7a-h). In addition, analysis of ChIP-seq of TBX5 from embryonic mouse
335 hearts [55] showed TBX5 occupancy at promoters of *Nppa, Slit2*, and *Ntn1* (Extended Data Fig. 8a-
336 c), suggesting these guidance genes are likely to be direct targets of TBX5 in the heart.
337
338 <u>*Tbx5-Slit2* and *Tbx5-Ntn1* genetic interactions.</u> We evaluated if genetic interactions existed
339 between *Tbx5* and *Slit2* or *Ntn1* (Extended Data Fig. 9). As *Tbx5* heterozygous mutant (*Tbx5*$^{del/+}$)
340 [45] mouse embryos display muscular or membranous VSDs, we wondered if heterozygous *Slit2* or
341 *Ntn1* loss of function (LOF) mutant embryos might alter *Tbx5*-dependent phenotypes. We mated
342 *Tbx5*$^{del/+}$ mice with either *Slit2* (*Slit2*$^{+/-}$) or *Ntn1* (*Ntn1*$^{beta\text{-}actin\text{-}Cre/+}$ referred here subsequently as
343 *Ntn1*$^{+/-}$ [56,57]) heterozygous LOF mice. In *Tbx5*$^{del/+}$ embryos at E14.5, we observed membranous
344 (n=5/8) or muscular (n=3/8) VSDs by histology (Extended Data Fig. 9a, b, e), consistent with
345 previous reports [45]. Among *Slit2*$^{+/-}$ embryos at E14.5, we observed a membranous VSD (n=1/8)
346 (Extended Data Fig. 9c, e). This contrasted with a previous report that did not detect any VSDs in

347 *Slit2*$^{+/-}$ albeit using a different mutant *Slit2* allele [49]. In *Tbx5*$^{del/+}$;*Slit2*$^{+/-}$ compound heterozygous
348 embryos, we observed a non-significant effect on the reduction of membranous VSDs (n=5/8)
349 (log OR -2.5; p=0.09 in a Generalized Linear Model without adjustments for multiple comparisons)
350 (Extended Data Fig. 9d, e), relative to the expected incidence of membranous VSDs if there was
351 no genetic interaction between *Tbx5* and *Slit2*.

352 We next tested if there was a genetic interaction between *Tbx5* and *Ntn1* (Extended Data
353 Fig. 9f-j). In *Ntn1*$^{+/-}$embryos, we observed a membranous (n=1/9) or a muscular (n=1/9) VSD. In
354 *Tbx5*$^{del/+}$;*Ntn1*$^{+/-}$ compound heterozygous embryos, we observed a significant decrease of
355 membranous VSDs (n=1/8; log OR -5.3; p=1x10^{-3} by a Generalized Linear Model without
356 adjustments for multiple comparisons), relative to the expected incidence of membranous VSDs
357 if there was no genetic interaction between *Tbx5* and *Ntn1,* but not significant changes to
358 prevalence of muscular VSDs (n=4/8; log OR 0.12; p=0.93), consistent with a genetic interaction
359 between *Tbx5* and *Ntn1* for ventricular septation.

360 We wondered if there were other quantitative histologic differences, in addition to the
361 changes in incidence of VSD types. To quantify morphometry from histology, we leveraged a
362 deep learning algorithm, known a CODA [58], to detect embryonic mouse heart components from
363 hematoxylin and eosin (H&E) sections. We generated three-dimensional (3-D) tissue
364 reconstructions, to visualize and quantify anatomic structures and CHDs, including membranous
365 and muscular VSDs, at cellular resolution (Fig. 6a-e). Using this machine learning method, we
366 discovered that the cell density of the IVS, which we termed IVS fill, was increased in *Tbx5*$^{del/+}$;
367 *Ntn1*$^{+/-}$ embryos compared to wildtype (p<0.05 by Fisher's exact test), while classification of the
368 IVS as trabecular was significantly reduced in *Tbx5*$^{del/+}$;*Ntn1*$^{+/-}$ embryos (p<0.05 by Fisher's exact
369 test) (Extended Data Fig. 9m). In addition, we estimated the minimal area for each membranous
370 or muscular VSD, when present (Extended Data Fig. 9o, p). In *Tbx5*$^{del/+}$;*Slit2*$^{+/-}$ compound
371 mutants, we detected statistically significant levocardia (p<0.001 by Fisher's exact test), as

372 determined by the axis of the heart compared to the spine and sternum (Extended Data Fig. 9q).
373 This uncovered a genetic interaction between *Tbx5* and *Slit2* related to heart position,
374 demonstrating that machine learning-based morphometry can quantify unexpected anatomic
375 findings.
376
377 *Slit2* and *Ntn1* for ventricular septation. To determine if *Slit2* or *Ntn1* are essential for ventricular
378 septation, we evaluated homozygous LOF mouse mutants for *Slit2* or *Ntn1* for VSDs. In *Slit2*$^{-/-}$
379 embryos at E14.5, we observed that homozygous loss of *Slit2* displayed complete penetrance for
380 VSDs, including membranous (n=3/4; log OR 5.0, p=0.02 by a Generalized Linear Model) or
381 muscular VSD (n=1/4) (Fig. 6f-i). We detected a statistically significant non-compacted IVS, which
382 was determined by reduced IVS fill, and thinning of the right ventricular compact layer, and we
383 quantified the area of membranous VSDs (Extended Data Fig. 10e-k). In addition, *Slit2*
384 heterozygous LOF displayed an increase of membranous VSDs (n=1/8, OR 2.5, p=0.02 by a
385 Generalized Linear Model), relative to the expected incidence of membranous VSDs in controls.
386 This demonstrated a far higher incidence of VSDs in *Slit2* mutants than reported using an
387 alternative *Slit2* LOF allele [49].
388 *Ntn1* homozygous LOF embryos displayed an increase of membranous VSDs (n=6/7; log
389 OR 6.32, p=0.0052 by a Generalized Linear Model without adjustments for multiple comparisons)
390 that we quantified by area, while other morphometry parameters were not significant (Extended
391 Data Fig. 10f-r). *Ntn1* heterozgyous LOF embryos were enriched for membranous VSDs (n=1/9,
392 OR 3.17, p=0.0052 by a Generalized Linear Model), relative to the expected incidence of
393 membranous VSDs in controls. Collectively, this morphologic evidence implicates *Slit2* and *Ntn1*
394 in proper ventricular septation during heart development.
395 As *Slit2* and *Ntn1* were necessary for ventricular septation, we asked if loss of *Slit2* or
396 *Ntn1* might disturb distribution of the *Tbx5*$^{+}$/*Mef2cAHF*$^{+}$ lineage in the IVS. In homozygous *Slit2*

397 LOF mutants with the lineage reporter (*Tbx5*$^{CreERT2/+}$;*Mef2cAHF-DreERT2*;*ROSA26*$^{Ai66/+}$;*Slit2*$^{-/-}$),
398 we observed a statistically-significant broadened distribution of the *Tbx5*$^{+}$/*Mef2cAHF*$^{+}$ lineage
399 compared to controls (Fig. 6n-r), consistent with lineage mixing from boundary disruption and
400 implicating a role for SLIT2 in maintaining boundary integrity. Conversely, homozygous *Ntn1* LOF
401 mutants with the lineage reporter (*Tbx5*$^{CreERT2/+}$;*Mef2cAHF-DreERT2*; *ROSA26*$^{Ai66/+}$;*Ntn1*$^{-/-}$)
402 demonstrated leftward displacement of the *Tbx5*$^{+}$/*Mef2cAHF*$^{+}$ lineage compared to controls (Fig.
403 6s-v), implying that NTN1 signaling precisely positions the compartment boundary at the IVS.
404 Taken together, this evidence suggested that SLIT2- and NTN1-signaling, as part of a Tbx5-
405 dependent pathway, regulates the position and integrity of the compartment boundary labeled by
406 the *Tbx5*$^{+}$/*Mef2cAHF*$^{+}$ lineage (Fig. 6w).
407
408 Discussion. We show that *Tbx5*$^{+}$/*Mef2cAHF*$^{+}$ progenitors prefigure a compartment boundary that
409 becomes located at the junction between the left and right sides of the IVS, providing a cellular
410 framework during development for heart patterning. Our study underscores a fundamental
411 principle that early developmental events preconfigure structure and function of the heart and are
412 susceptible to genetic risks that cause CHDs. Further, our results demonstrate developmental
413 regulation of a compartment boundary by a disease-associated TF and that aberrant tissue
414 patterning from boundary disturbances may be an etiology of birth defects. This study reiterates
415 the importance of compartment boundaries in tissue patterning, provides evidence for
416 compartment boundary disruptions as an etiology of birth defects, and adds to the few examples
417 of compartment boundaries that exist in mammals.
418 We surmise that the rarity of compartment boundaries in mammals likely stems from a few
419 reasons. The discovery of a compartment boundary was made by studying the fate of marked
420 mosaic cells and their clonal segregation in the wing disk of the fly embryo [59]. Subsequent
421 examples of compartment boundaries were identified by broad genetic screens in *Drosophila* [60].

422 In mammals, compartment boundaries were discovered by lineage analysis informed by another
423 organism [33] or serendipitously [30], as we have done here. Compartment boundaries have been
424 defined by several criteria. First, a compartment boundary segregates juxtaposed cell populations
425 such as distinct cell lineages to restrict cell intermingling, and ablation of the boundary leads to
426 cell mixing. Second, the expression domain of a selector gene corresponds with a compartment
427 domain, loss of the selector gene eliminates the identity in this territory, and ectopic expression
428 of the selector induces this identity. Third, a selector gene establishes a signaling center to
429 maintain the compartments and boundary. Our results satisfy all of these criteria: Ablation of the
430 *Tbx5*$^{+}$/*Mef2cAHF*$^{+}$ lineage disrupts segregation of *Tbx5*$^{+}$ lineage cells in the LV from the *Tbx5*$^{-}$
431 lineage in the RV of the developing heart. Reduced *Tbx5* expression impairs the integrity of the
432 boundary and its patterning, and in previous work misexpression of TBX5 eliminates IVS
433 formation [13]. Third, TBX5 patterns signaling molecules that are important for morphologies that
434 impact the boundary. In this context, we postulate that *Tbx5* may function as a candidate selector
435 gene. Further experiments will be needed to formally ascertain this.

436 In this context, we identify a *Tbx5*-dependent pathway that regulates *Slit2* and *Ntn1*.
437 Normally, TBX5 represses their ectopic expression in the IVS and compact layer. Both SLIT2 and
438 NTN1 are guidance or adhesive cues in several developmental contexts. Complete loss of *Slit2*
439 causes perinatal lethality (Plump et al., 2002). *Ntn1*$^{-/-}$ die around E11.5 [61] or E14.5 [56]. Between
440 E10.5 and E14.5, homozygous *Ntn1*$^{-/-}$ embryos exhibited absence of ventral spinal commissure,
441 and disorganized dorsal root entry zone [56].

442 Here, we provide evidence that *Slit2* and *Ntn1* are direct targets of TBX5, and that *Tbx5*
443 and *Slit2* or *Ntn1* genetically interact. Further, we found that *Slit2* and *Ntn1* are essential for proper
444 ventricular septation, as well as compartment boundary integrity and positioning, respectively.
445 Like TBX5, proper ventricular septation may be sensitive to imbalanced dosage of SLIT2 or NTN1.
446 Of note, mutations of *SLIT2* and the SLIT-receptor *ROBO1* are associated with CHDs in mouse

447 and humans [49–52]. For NTN1, knockdown of *ntn1a* in zebrafish results in cardiovascular
448 abnormalities [53], while *NTN1* had not yet been clearly implicated as a risk gene for mouse [61] or
449 human CHDs [53]. Even so, *DSCAM*, which encodes a NETRIN co-receptor, is in the risk region for
450 Trisomy 21 [62], which often includes atrioventricular septal defects. Moreover, single nucleotide
451 variants in *NEO1* and *UNC5B*, which encode NTN-receptors, are associated with CHDs [63,64]. As
452 mouse embryos from *Unc5b* loss, formerly known as *Unc5h2*, died of vascular abnormalities of
453 the placenta by E12.5 [65,66], it remains unclear what role *Unc5b* might have in cardiac chamber
454 formation and ventricular septation. As *Ntn1* expression is enriched in the LV and left-side of the
455 IVS in the *Tbx5*$^{+}$ compartment, we propose a working hypothesis that NTN1 may function as a
456 TBX5-dependent signaling center for compartment boundary regulation.

457 The spatiotemporal position of the boundary is at the crux of cardiac septation and, when
458 disrupted, spans sites for congenital cardiac anomalies. The sensitivity of the *Tbx5*$^{+}$/*Mef2cAHF*$^{+}$
459 lineage-labeled boundary to genetic perturbations, specifically *Tbx5* deficiency, is of significance
460 in the context of CHDs. Such deficiency selectively compromises the boundary's integrity and
461 position, along with disturbances to cell orientation, leading to VSDs or AVSDs. These
462 observations suggest that patterning during heart morphogenesis is exceptionally vulnerable to
463 disruptions of gene dosage in early cardiac precursors. Early susceptibility could explain why
464 CHDs arise at higher frequency than other birth defects. Thus, the *Tbx5*$^{+}$/*Mef2cAHF*$^{+}$ lineage
465 provides a potential “beacon” for understanding the cellular basis of septation defects. Whether
466 additional genetic perturbations that cause VSDs or AVSDs disrupt the compartment boundary
467 remains to be determined. Likewise, it will be interesting to evaluate if the *Tbx5*$^{+}$/*Mef2cAHF*$^{+}$
468 lineage-labeled boundary corresponds with abnormal shifts in IVS position, like those observed
469 in the endothelial loss of *Hand2*, which displays rightward shifted IVS and double inlet left ventricle
470 (DILV) or two IVS primordia [67,68].

471 Several limitations of this study should be considered. Using inducible genetic tracing,
472 there is an inherent variability from recombination of the fluorescent reporters within samples. For
473 some comparisons, more samples of each genotype could have mitigated this limitation, but
474 obtaining additional samples have been technically challenging, in large part due to a requirement
475 of 5 alleles to be present. Notwithstanding, we have tried to account for recombination efficiency,
476 when possible, in imaging analyses. We have made great effort to mitigate this concern by not
477 quantifying measurements that would be greatly skewed by recombination efficiency. For this
478 reason, for example, we have refrained from commenting on whether a given lineage is
479 quantitatively increased or decreased if fewer samples were available. Instead, we have focused
480 our analyses on the location of the cells, as we feel that this is less affected by recombination
481 efficiency. Using orthogonal approaches, we measure in an unbiased and statistically robust
482 fashion using various metrics of quantitative morphometry from lightsheet or histology images.
483 Our interpretations are based on statistical robustness from a large number of sampled regions
484 per embryo, in the comparisons that are presented. The repeated measurements are akin to the
485 (much larger) measurements in single cell RNAseq.

486 Broadly, our research demonstrates the delicate interplay of progenitor cell behavior, gene
487 expression and compartment boundary formation that determines heart development and genetic
488 susceptibility that increases the risk of CHDs. This evidence further underscores the significance
489 of early developmental stages for the ontogeny of some CHDs. Whether the extent of interaction
490 between progenitor fields, migration of heart progenitors, or formation of the boundary may
491 contribute stochastically to phenotypic variation observed as a frequent feature of CHD genetics
492 in mice or humans remains unclear. The implications of these discoveries likely extend beyond
493 cardiac morphogenesis, as these findings offer insights for the roles of compartment boundaries
494 during mammalian development and uncover a vulnerability for organ patterning from genetic
495 disturbances.

496

497 **Methods.**

498 Mouse Lines. All mouse protocols (AN203375-00H and AN199784-00E) were approved by the
499 Institutional Animal Care and Use Committee at UCSF. Mice were housed in a barrier animal
500 facility with standard husbandry conditions at the Gladstone Institutes. Mice of
501 *Tbx5*^{CreERT2IRES2xFLAG} (abbreviated here as *Tbx5*^{CreERT2}) and *Mef2cAHF-DreERT2* [25], *Tbx5*$^{del/+}$ and
502 *Tbx5*$^{flox/+}$ [45], *ROSA26*^{Ai66} and *ROSA26*^{Ai6} [35] were described previously. *Mef2cAHF-Cre* mice [46]
503 were obtained from Brian Black (University of California, San Francisco). *Slit2*$^{+/-}$ mice (MMRC,
504 Strain 065588-UCD, donated by Kent Lloyd, UC Davis) were generated by CRISPR/Cas9-
505 targeted constitutive deletion of exon 8 and flanking splicing regions of *Slit2*. *Ntn1*$^{+/-}$ mice
506 were derived from matings of *Ntn1* floxed mice (*Ntn1*$^{flox/+}$; Jackson Laboratory #028038) [56]
507 to *beta-actin-Cre* [57], which were obtained from Gail Martin (University of California, San
508 Francisco). All mouse strains were maintained in the C57BL6/J background (Jackson Laboratory
509 #664), except for *Tbx5*$^{del/+}$, which was maintained in Black Swiss (Charles River, Strain Code
510 492), and *Slit2*$^{+/-}$ which was maintained in C57BL6/N (Jackson Laboratory, #005304). Both male
511 and female embryos were collected from timed matings and used at random for experiments.
512 Tamoxifen (Sigma-Aldrich; T5648) was suspended in sesame oil at 10mg/ml. The injected dose
513 was 100ug per 1 gram of body weight.

514

515 Cloning and Generation of Mouse Lines. We generated an attenuated diptheria toxin (DTA176)
516 transgenic knock-in mouse under the control of the dual-recombinase intersectional cassette.
517 DTA176 encodes an attenuated form of toxic fragment A from diptheria toxin [36,37], which requires
518 ~100-200 molecules for cell killing. This strategy was an effort to reduce potential problems of
519 leaky DTA expression prior to recombinase-mediated activation. Briefly, *DTA176* [37] was cloned
520 downstream of ROX-STOP-ROX and LOX-STOP-LOX sites to create a Dre- and Cre-dependent

521 expression construct, which was derived from the Dre- and Cre-dependent tdTomato expression
522 cassette of the Ai66 (RCRL-tdT) targeting vector [35]. After the tdTomato cassette was removed
523 using MluI sites and replaced by DTA176, the construct was cloned into the TARGATT targeting
524 construct pBT346.3 (Applied Stem Cells) to target the transcriptionally inactive *Hip11* locus [69]
525 using PacI and SmaI restriction enzyme sites. The final construct was verified using restriction
526 digestion and Sanger sequencing. DNA was purified and injected along with mRNA for the Phi31o
527 transposase according to manufacturer's protocol to generate intersectional-DTA mutant
528 (*Hip11*$^{Rox\text{-}STOP\text{-}Rox\text{-}Lox\text{-}STOP\text{-}Lox\text{-}DTA176}$) mice. To generate Ai66b mice (*ROSA26*^{Ai66b}), which is a Dre-
529 dependent tdTomato reporter, the LOX-STOP-LOX sites were removed from the Ai66 (RCRL-
530 tdT) targeting vector [35], and then the transgene cassette was inserted into endogenous genomic
531 loci via homologous recombination, as previously described [70].
532
533 Whole Mount Embryo and Heart Immunofluorescence Labeling. Embryos were dissected from
534 timed pregnant dams, including removal of yolk sac for genotyping, as previously described [25].
535 Embryos staged up to E10.5 were fixed for 4 hours in 4% PFA at room temperature, then
536 incubated with gentle rocking in clearing solution (8% SDS in 0.2M sodium borate buffer, pH 8.5)
537 at 37°C for 1-3 hours until clear. E13.5 to E14.5 hearts were micro-dissected from freshly
538 harvested embryos in PBS with heparin (10 Units/mL) (Sigma #H3393) or incubated in 1X RBC
539 lysis solution (Roche #11814389001) for 10 minutes at room temperature, fixed at room
540 temperature in 4% PFA for one hour, and incubated with gentle rocking in clearing solution at
541 37°C for 2-4 days until clear. Specimens were permeabilized and blocked for two hours to
542 overnight with gentle rocking at 37°C in blocking buffer (PBS containing 5% normal donkey serum
543 and 0.8% to 1.5% Triton X-100, dependent on embryo/heart stage). Specimens were labeled with
544 primary antibody (list below) in blocking buffer with gentle rocking at 37°C, either overnight for
545 embryos with stages up to E10.5, or for 5 days for E13.5 or E14.5 hearts. For long incubations,

546 antibody solution was replaced halfway. Following three washes in blocking buffer, each 45
547 minutes except the third overnight for E13.5 and E14.5 hearts, specimens were incubated with
548 secondary antibody (raised in donkey; AF488-, Dy405-, Cy3, or AF647-conjugated; used at 1:750;
549 Jackson ImmunoResearch) and DAPI in blocking buffer with gentle rocking at 37°C, 2-3 hours for
550 embryos up to E10.5, or 5 days for E13.5 or E14.5 hearts. Following three washes in PBS with
551 gentle rocking at 37°C, samples were stored (up to overnight) in PBS with 0.2% sodium azide.
552 Primary antibodies used were: tdTomato (rabbit, Rockland 600-401-379, 1:1000), MEF2c (sheep,
553 R&D AF6786, 1:250), TNNT2 (mouse, Thermo MS-295-P, 1:500). Strong ZsGreen fluorescence
554 persisted after clearing and did not require immunolabeling.
555
556 Lightsheet Image Acquisition. Images were acquired by lightsheet microscopy, as described
557 previously [71]. Brielfy, specimens were warmed and transferred to 2% low melting point agarose
558 (Fisher BP165-25) in PBS at 37°C, then embedded in glass capillary tubes with paired pistons
559 (Sigma Z328510 paired with BR701938, or Sigma Z328502 paired with BR701934) for embryos,
560 or tip-truncated 1mL syringes (Becton Dickinson) for hearts. After the gel solidified, the capillaries
561 or syringes were suspended specimen-down from 14mL polystyrene tubes sealed with Parafilm.
562 Columns containing the specimen were partially extended into an ample volume optical clearing
563 solution (OCS, EasyIndex EI-Z1001, LifeCanvas) overnight. Following overnight incubation in
564 OCS, specimen capillaries were retracted, and were brought to a LightSheet Z.1 microscope
565 coupled with standard-issue laser lines and filter configurations, as well as dual pco.edge 4.2
566 cameras, with ZEN software (Carl Zeiss Imaging). Using immersion in OCS, specimens were
567 imaged with a multi-view whole-volume approach, using one of two objective setups: EC Plan
568 Neofluar 5X/0.16 with 5X/0.1 pair (hearts), or Clr Plan Neofluar 20X/1.0 paired with 10X/0.2
569 clearing pair (embryos). Z-stacks were collected at each view angle at the optimal slice thickness
570 determined by Zeiss' Zen software, ranging from 1.42 to 4.95 μm.

571

572 Image Dataset Preprocessing. Imaging data was processed, as previously described [71]. All data
573 processing was performed on an 8-core x86-64 desktop PC with 64GB RAM, running Kubuntu
574 20.04 LTS, principally using Fiji software [72]. Acquired lightsheet image stacks were subjected to
575 single-view deconvolution using regularized generalized Tikhonov filtering (Parallel Spectral
576 Deconvolution, https://imagej.net/plugins/parallel-spectral-deconvolution) following theoretical
577 PSF calculation using the intersection of Gaussian z-plane illumination with Gibson-Lanni
578 widefield epifluorescence detection patterns [73]. Deconvolved stacks were co-registered, and
579 image volumes were generated for each desired orientation, for each specimen, using Content
580 Based Fusion in BigStitcher [74]. TrackMate [75] and ImageJ 3-D viewer were used for segmentation
581 and visualization of fused volumes.

582

583 Image Volume Quantification. Extensive whole-volume quantifications of imaged E14.5 hearts
584 were performed using Fiji and associated plugins, with analysis conducted with R. For assessing
585 the location of fluorescence signal, volumes were downsampled, and 2-dimensional regions of
586 interest (ROIs) corresponding to anatomic structures were manually drawn on each Z-slice, using
587 the DAPI channel in a single blinded fashion. Integrated intensity for each fluorescence channel
588 was programatically measured for each ROI, and counts were normalized to DAPI signal and
589 pooled by anatomic region. For whole-heart quantifications, counts were further normalized to
590 combined Ai6 plus Ai66 signal, then averaged across each anatomic region. For orientation
591 assessments, a multi-channel panel of 174 full resolution four-chamber image excerpts, evenly
592 distributed between apical-posterior, apical-anterior, posterior-basal, and posterior-apical IVS,
593 were split by channel (tdTomato or ZsGreen) and blindly sampled. Using automated batch
594 processing, these samples were subjected to automated background filtering, including contrast
595 enhancement, and measurements of orientation coherency (OrientationJ plugin,

596 https://github.com/Biomedical-Imaging-Group/OrientationJ), and of dominant direction and
597 "directionality" score (Directionality plugin, https://github.com/fiji/Directionality). Directionality
598 score distributions were rotated so that dominant direction was set to 0°, with average score
599 (across the panel of images) was plotted as a function of direction, with testing of the distribution
600 by the Watson U2 test (R circular package) and analyzed by Watson's two-sample test. Individual
601 scores surrounding 0° (±5°), 90° (±5°), and 65° (±20°) were pooled and compared with the
602 Wilcoxon signed-rank test. An alternative measure, orientation coherency scores, across the
603 panel of images were plotted by genotype and compared with the Wilcoxon signed-rank test.
604
605 Quantification of Right-Left Position of Lineages. For each E10.5 heart analyzed, five
606 representative coronal optical sections were selected, approximately 20-35 μm apart. For each
607 optical section, the DAPI channel was used to draw five linear profiles spanning the ventricular
608 chambers from right to left. Linear profiles were drawn such that the "0" position corresponded to
609 the midline, identified by the interventricular groove. Fluorescence intensity of each channel
610 (green=*Tbx5*$^{+}$ lineage, magenta=*Mef2cAHF+* lineage) was measured along each linear profile,
611 and intensity values were normalized to the maximum value along each profile. Profiles for each
612 channel were grouped by experimental condition (WT or DTA), and then the average ± SEM
613 normalized fluorescence intensity profiles were calculated and plotted. Welch's two-sample t-test
614 was used at each position along the right-left axis to determine regions of significant difference in
615 fluorescence intensity of each channel between experimental groups, indicating a change in the
616 distribution of cells of that lineage.
617 The same images and Z-slices were also analyzed for the percent distribution of the
618 green=*Tbx5*$^{+}$ and pink=*Mef2c-AHF*$^{+}$ lineages across the ventricles. ROIs were assigned using the
619 DAPI channel to subset the left and the right ventricles using the IV groove as a landmark. The
620 percent area was calculated using the area of the green or red signal and the total ventricular

621 area. These values were normalized per Z-slice to the total area of signal in both ventricles.
622 Significance was measured using T-tests.

623 For each E13.5-E14.5 heart analyzed, maximum z-projections were generated from
624 optical sections spanning every 50 μm (E13.5-E14.0) or 100 μm (E14.5) from the anterior to
625 posterior of the heart. For each maximum z-projection, the DAPI and red or magenta
626 (*Tbx5*$^{+}$/*Mef2cAHF*$^{+}$ intersectional lineage) channels were split and background subtraction was
627 performed on the red or magenta channel using a 50-pixel rolling ball radius. The DAPI channel
628 was used to draw three linear profiles (basal, middle, apical) spanning the ventricular chambers
629 from right to left. Linear profiles were drawn such that the "0" position corresponded to the middle
630 of the IVS. Fluorescence intensity of the red or magenta channel was measured along each linear
631 profile, and intensity values were normalized to the maximum value along each profile. Profiles
632 were grouped by experimental condition (*Tbx5*$^{CreERT2/+}$ or *Tbx5*$^{CreERT2/flox}$) or (e.g. WT, *Ntn1*$^{+/-}$, *Ntn1*$^{-}$
633 $^{/-}$) and then the average ± SEM normalized fluorescence intensity profiles were calculated and
634 plotted. Two sample F-test and Welch's t-test were used to analyze the distribution of
635 *Tbx5*$^{+}$/*Mef2cAHF*$^{+}$ intersectional lineage cells.

636

637 <u>Cell Harvesting for Single Cell RNA Sequencing.</u> Samples for single cell RNA sequencing were
638 collected from three independent litters at E13.5. The heart was microdissected to obtain the
639 interventricular septum (IVS), left ventricular (LV) and right ventricular (RV) regions. Control
640 samples were *Tbx5*$^{CreERT2/+}$*;Mef2cAHF-DreERT2;ROSA26*$^{Ai66/Ai6}$ (n=3) and
641 *Tbx5*$^{CreERT2/+}$*;Mef2cAHF-DreERT2;ROSA26*$^{Ai66/+}$ (n=1) for LV, RV and IVS each. *Tbx5* mutant
642 samples were *Tbx5*$^{CreERT2/flox}$*;Mef2cAHF-DreERT2;ROSA26*$^{Ai66/Ai6}$ for RV and LV (n=3 each) and
643 IVS (n=2). One *Tbx5* mutant sample of the IVS+AV complex regions was not included because it
644 was lost from a microfluidic chip clog during sample processing.

645 Each microdissected tissue was singularized with TrypLE Express (Life Technologies,
646 Cat# 12604-013) at 37C and quenched with 1% FBS in PBS. The single cell suspension was then
647 filtered through a cell strainer cap (Corning, Cat# 352235) and centrifuged at 300g for 5 minutes.
648 The pellet was resuspended in 1% FBS in PBS and counted using an automated cell counter. A
649 30µL aliquot of the cell suspension was used to generate single cell droplet libraries with the
650 Chromium Next GEM Single Cell 5' Library & Gel Bead Kit v1.1, according to manufacturer's
651 instructions (10X Genomics). After KAPA qPCR quantification, a shallow sequencing run was
652 performed on a NextSeq 500 (Illumina) prior to deep sequencing on a NovaSeq S4 (Illumina). For
653 control IVS+AV complex regions, at E13.5, 3 samples were *Tbx5*$^{CreERT2/+;}$*Mef2cAHF-*
654 *DreERT2;ROSA26*$^{Ai66/Ai6}$
655
656 Data Processing Using Cellranger. All datasets were processed using Cellranger 2.0.2. FASTQ
657 files were generated using the mkfastq function. Reads were aligned to a custom mm9 reference
658 (version 1.2.0) containing tdTomato and ZsGreen reporter genes. Cellranger aggr was used to
659 aggregate individual libraries after read depth normalization.
660
661 Seurat Analysis. Outputs from the Cellranger pipeline were analyzed using the Seurat v3 [76–78].
662 Datasets from the IVS, LV and RV were analyzed separately. Cells with 10,000-50,000 UMIs and
663 1500-7250 genes were retained. Data was normalized using the NormalizeData function and
664 scaled using ScaleData, while also regressing unwanted sources of variation, such as differences
665 in the number of UMIs, number of genes, percentage of mitochondrial reads and differences
666 between G2M and S phase scores. Principal component analysis (PCA) was performed using the
667 most highly variable genes. Cells were then clustered based on the top 30 principal components
668 and visualized on a Uniform Manifold Approximation and Projection (UMAP) [79]. A clustering
669 resolution that separated cells by major cell types was chosen. Next, *Tnnt2*$^{+}$ clusters from the IVS

670 dataset were extracted and re-clustered, similar to the parent dataset above. A clustering
671 resolution was chosen based on separation of genotypes. Differential gene expression tests
672 between clusters or between *ZsGreen*$^{+}$ and *ZsGreen*$^{-}$ or *tdTomato*$^{+}$ and *tdTomato*$^{-}$ cells were
673 performed using the FindMarkers function with default parameters. Selected differentially
674 expressed genes with an adjusted p-value less than 0.05 from the Wilcoxon rank sum test were
675 displayed using the Dotplot or FeaturePlot functions.
676
677 Fluorescent *In Situ* Hybridization. E11.5 or E14.5 hearts were fixed with 4% paraformaldehyde or
678 10% formalin overnight at 4C, embedded in paraffin and then sectioned for a transverse or four-
679 chambered view on slides. *In situ* hybridization was performed on sections using the RNAscope
680 Multiplex Fluorescent v2 Assay kit (Advanced Cell Diagnostics, Cat# 323100). Briefly, sections
681 were deparaffinized in xylene and 100% ethanol, treated with hydrogen peroxide for 10 minutes
682 and boiled in target retrieval buffer for 10 minutes. A hydrophobic barrier was drawn around each
683 section using an Immedge pen (Vector Laboratories, Cat# H-4000), and slides were allowed to
684 dry overnight. The following day, sections were treated with Protease Plus for 30 minutes,
685 followed by hybridization with probes for 2 hours at 40C. Probes (Advanced Cell Diagnostics)
686 used were *Mm-Tnnt2-C4* (Cat# 418681-C4), *Mm-Ntn1* (Cat# 407621), *Mm-Slit2* (Cat# 449691),
687 *Mm-Nppa-C3* (Cat# 418691-C3), *Mm-Bmp2-C2* (Cat# 406661-C2), *Mm-Robo1* (Cat#475951),
688 *Mm-Unc5b* (Cat#482481), and *Mm-Irx2* (Cat#519901). Amplification steps were carried out
689 according to manufacturer's instructions. Opal dyes 520, 570, 620 and 690 (Akoya Biosciences,
690 Cat# FP1487001KT, FP1487001KT, FP1487001KT and FP1487001KT) were used at 1:750
691 dilution. After staining with DAPI, 1-2 drops of ProLong Gold Antifade Mountant (ThermoFisher
692 Scientific, Cat# P36930) were placed on the slides and mounted with a coverslip. Slides were
693 stored overnight at 4C and were imaged at 10X magnification on the Olympus FV3000RS. Multi-

694 Area Time Lapse (MATL) images were captured and then stitched together using the Olympus
695 FV3000RS software. Stitched images were analyzed using ImageJ OlympusViewer plugin.
696
697 Immunohistochemistry. Cryopreserved slides were thawed from -80C at RT and washed in
698 0.1% Triton X-100 in PBS (PBST) for 3 x 5 min. Antigen-retrieval was performed by boiling
699 slides in 10mM sodium citrate buffer (pH 6.0) for 10 minutes and then washed in H2O for 3 x 5
700 min. Blocking was performed using 5% donkey serum in 0.1% PBST at RT for 1-2hr. Anti-
701 Netrin-1 antibody 1:500 (R&D Systems AF1109) in 1% BSA + 0.1% PBST was incubated at 4C
702 overnight. After washing 3 x 5 min in 0.1% PBST, slides incubated in Alexa Fluor 594 (1:300) in
703 1% BSA + 0.1% PBST at RT for 1 hr. Slides were then washed 3 x 5 min in 0.1% PBST and
704 incubated in 1:1000 DAPI in 0.1% PBST at RT for 5-10 minutes. Finally, slides washed 3 x 5
705 min in 0.1% PBST, glass coverslips were mounted using Prolong Gold antifade mounting
706 medium and stored at 4C.
707
708 Quantification of IVS Cell Size and Shape by WGA Staining. Blind measurements of
709 interventricular septum (IVS) cell size and shape were made on 5 µm paraffin-embedded
710 *Tbx5*$^{CreERT2/+}$ or *Tbx5*$^{CreERT2/flox}$ hearts at E14.5, sectioned in 4-chamber view approximately
711 midway in the anterior-posterior axis. After sectioning, slides were stained for cardiac troponin T
712 (cTNT, 1:500 cTNT, Thermo, MS-295-P) using Alexa 488 donkey anti-mouse secondary
713 antibody (Jackson Immunoresearch), in addition to Alexa 594 conjugated Wheat Germ
714 Agglutinin (WGA, dilution 5 µM, Thermo, W11262) and DAPI. After widefield imaging on a
715 confocal fluorescence microscope at 40X, regions of interest (ROIs) from apical, basal, and mid
716 regions of the IVS were extracted in both DAPI and WGA channels, guided by the cTNT
717 staining as an anatomic reference. ROIs from the DAPI channel were subjected to automatic
718 segmentation and counting to assess cell number and density. ROIs from the WGA channel

719 were scrambled for blinding *Tbx5* genotype, and 24 to 56 easily identified cell bodies per ROI
720 (depending on ROI size) were manually assessed in Fiji for length, width, and axis orientation.
721 Taking cell bodies as roughly elliptical, their diameter, area, and eccentricities were estimated,
722 and *Tbx5* genotype identities were unscrambled for plotting. Scripts for the filename
723 scrambling/unscrambling, as well as automated quantification and count tallying, as described
724 above, are available at Github (https://github.com/mhdominguez/Kathiriya-NCVR-2025-
725 analysis).
726
727 Machine Learning-Based 3-D Reconstruction from Histology and Quantitative Micrometry.
728 Tissues were formalin-fixed, paraffin embedded (FFPE) and serially sectioned at a standard
729 thickness of 5 μm to exhaustively collect the heart tissue of each fetal mouse. Serial sections
730 were stained with hematoxylin and eosin (H&E) and digitized at 20x magnification using a Leica
731 Versa 200 Automated Slide Scanner. CODA, a technique to 3-D reconstruct serial tissue images,
732 was used to map the microanatomy of the hearts [58,80]. The various steps of CODA can be broken
733 down into image registration, nuclear detection, and tissue labelling. Nonlinear image registration
734 was used to align the serial images. Cellular coordinates were generated through color
735 deconvolution and detection of two-dimensional intensity peaks in the hematoxylin channel of the
736 images. A deep learning semantic segmentation algorithm was trained to label the anatomical
737 structures of the mice at 1 μm resolution. To train the model, manual annotations of six structures
738 were generated in 55 histological images corresponding to the different large structures present
739 in the tissue: bones, spinal cord, lung, liver, stroma, heart, and non-tissue pixels in the images. A
740 second deep learning model was trained to subclassify the regions of interest within the heart:
741 compact myocardium, trabeculae, IVS, AV complex region, and atria. Fifty images from the
742 manual annotation datasets were used for model training, with five images held out for
743 independent testing of model accuracy. The models were deemed acceptable when they reached

744 a minimum per-class precision and recall of >85%. Using the trained model, independent images
745 were segmented and aligned to generate digital 3-D datasets.
746 The reconstructed volumes enabled microanatomical quantification of anatomical
747 properties. IVS fill, or the solidity of the muscle layer in the IVS, was calculated by dividing the
748 number of dark (<200 in RBG color space) pixels within the IVS, normalized by all pixels (including
749 empty space) within the IVS. Percent trabeculation within the IVS was calculated by isolating the
750 tissue classified as trabeculae that was spatially attached to the IVS, then normalizing this number
751 by the combined volume of trabeculae attached to IVS and the volume of the IVS itself. The
752 compact myocardium thickness was calculated by measuring the thickness of the compact layer
753 at the bottom 20% of the ventricles. To measure the thickness on the left and right ventricles, the
754 two sides of the heart were manually segmented in 3-D space. VSDs were identified by calculating
755 regions where the empty space of the left ventricle contacted the empty space of the right
756 ventricle. These defects were evaluated and manually sorted into membranous or muscular sub-
757 types. The areas of each defect were then manually calculated through annotation on serial
758 histological images representing the shortest path to close the defect. These lines were summed
759 across all images containing the defect multiplied by the thickness of the histological slides to
760 determine the area of the hole.
761
762 Statistics and Reproducibility. For statistical analysis of genetic interactions, the number of
763 animals with a given defect (muscular VSD or membranous VSD) was modeled in a Generalized
764 Linear Model assuming a binomial probability distribution for the observed counts. This model
765 included main effects (in terms of log odds ratios) capturing the number of mutant alleles for *Tbx5*
766 (0 or 1, representing the WT or the Het genotype, respectively) and the number of mutant alleles
767 for *Slit2* or *Ntn1* (0,1 or 2: representing the WT, Het or Hom genotype, respectively) and an

interaction between these effects. Given the relatively small number of animals in this experiment, bias-reduced estimates were made using the brglm2 package {Kosmidis.2020} in R.

Representative images are shown based on experiments that were repeated independently with similar results, as follows: Figure(s) 1a-f: 2 samples; 1g-j: 5 samples; 2a-i: 4 samples; 2j-n: 6 samples; 2o-q: 8 samples; 2r-t: 15 samples; 3a,b: 2 controls, 2 *DTA* mutants; 3c-j: 2 controls, 4 *DTA* mutants; 3l-n' and Extended Data 2: 3 controls, 2 *DTA* mutants; 4a-d: 5 controls and 4 *Tbx5* mutants, for which some samples are shown in Extended Data Figure 4a-i; Figure 4i-m: 4 controls, 4n-r: 3 *Tbx5* mutants; 4u-v'; 2 controls, 2 *Tbx5* mutants; 5i-n; 2 controls and 2 *Tbx5* mutants, for which the second replicates are shown in Extended Data Figure 6i-n"; Figure 6f-h: 14 controls, 8 *Slit2*$^{+/-}$, 4 *Slit2*$^{-/-}$; 6j-l: 14 controls, 9 *Ntn1*$^{+/-}$, 7 *Ntn1*$^{-/-}$, with some samples shown in Extended Data Figure 10a-d; Extended Data Figure(s) 1: 2 samples per condition; 4a-l: 5 controls, 4 *Tbx5* mutants, with some samples shown in Figure 4; 3: 3 controls, 7 *Tbx5* mutants; 6a-h': 2 controls and 2 *Tbx5* mutants; 6o: 2 controls; 7a-h: 2 controls and 2 *Tbx5* mutants; 9a-d: 14 controls, 8 *Tbx5*$^{+/-}$, 8 *Slit2*$^{+/-}$; 8 *Tbx5*$^{+/-}$;*Slit2*$^{+/-}$; 9f-i: 14 controls, 7 *Tbx5*$^{+/-}$; 9 *Ntn1*$^{+/-}$, 7 *Ntn1*$^{-/-}$. Supplemental Figure(s) 1: 5 samples; 2: 5 controls, 4 *Tbx5* mutants; 3: 2 controls, 2 *Tbx5* mutants.

Data Availability. Source data is available upon publication. scRNA-seq data generated in this paper is available in the NCBI GEO database (GSE260601). ChIP-seq data from Akerberg et al., 2019, is available in the GEO database (GSE124008).

Code Availability.

Code related to "Image Volume Quantification" [71] is available at https://github.com/mhdominguez/LSFMProcessing. Source data and scripts used to analyze other morphometrics from lightsheet microscopy, such as right-left positioning, orientation and

792 directionality of cells, are available at https://github.com/mhdominguez/Kathiriya-NCVR-2025-
793 analysis.
794
795 **Acknowledgements**. We dedicate this manuscript in memory of Tatyana Sukonnik (Gladstone
796 Institutes). We thank Brian Black (University of California, San Francisco) for the *Mef2cAHF-Cre*
797 mouse line, and members of the Bruneau lab for troubleshooting help, discussions and
798 comments. We also thank the Gladstone Bioinformatics, Genomics, and Histology and
799 Microscopy Cores, the UCSF Laboratory for Cell Analysis, and the UCSF Center for Advanced
800 Technology. This work was supported by grants from the National Institutes of Health (NHLBI
801 Bench to Bassinet Program UM1HL098179 to B.G.B.; R01HL114948 to B.G.B., R01HL155906
802 to B.G.B. and I.S.K., 1R56HL166894-01A1 to I.S.K., K99HL177318 to J.M.M-V, U54CA268083
803 and UG3CA275681 to A.L.K.), also by a postdoctoral fellowship from the American Heart
804 Association, together with The Children's Heart Foundation (24POST1191660) to J.M.M.-V.,
805 Additional Ventures Innovation Fund to B.G.B., Society for Pediatric Anesthesia (Young
806 Investigator Award to I.S.K.), Hellman Family Fund (I.S.K.), UCSF REAC Grant (I.S.K.), UCSF
807 Pediatric Heart Center Catalyst Award to I.S.K. and UCSF Department of Anesthesia and
808 Perioperative Care Research Support to I.S.K. This work was also supported by an NIH/NCRR
809 grant (C06 RR018928) to the J. David Gladstone Institutes, and the Younger Family Fund
810 (B.G.B.).
811
812 **Author Contributions Statement.** W.P.D. and B.G.B. originally conceived, and I.S.K. and B.G.B.
813 refined and developed the study. W.P.D. made initial observations using genetic lineage tools
814 that he gathered or generated. I.S.K., M.H.D., W.P.D. and K.M.H. performed embryo dissections.
815 K.M.H., B.I.G., P.G., M.N.M., T.S., D.M.P., S.W. and E.F.B. managed animal husbandry and
816 genotyping. I.S.K., M.H.D., W.P.D. and K.M.H. performed whole mount or section immunostaining

experiments and imaging. M.H.D., J.M.M. and D.Q performed lightsheet imaging and processing, and M.H.D. and J.M.M. implemented analyses with hypothesis-based input from I.S.K. I.S.K. designed the strategy to use 5' sequencing kit and developed synthetic genome with Gladstone Bioinformatics core, micro-dissected heart regions for scRNA-seq and processed samples with K.S.R. and P.G. for sequencing library preparations. K.S.R. generated scRNA-seq libraries and performed scRNA-seq analyses with hypothesis-based input from I.S.K. K.S.R., K.M.H., P.G. and M.N.M. performed section *in situ* hybridization and imaging. K.S.R. generated ChIP-seq browser tracks with input from S.K.H. I.S.K. assessed cardiac defects by histology and provided anatomical knowledge to A.L.K. to apply a deep learning tool for cardiac morphometry. A.F. trained deep learning models and was supervised by A.L.K. and advised by P-H.W. and D.W. B.G.B. supervised and advised the study. I.S.K. and K.S.R. prepared figures. I.S.K. wrote the original draft with contributions from co-authors. I.S.K. and B.G.B. edited the manuscript with input from co-authors.

Competing Interests Statement. B.G.B. is a co-founder and shareholder of Tenaya Therapeutics. B.G.B. is an advisor for Silver Creek Pharmaceuticals. None of the work presented here is related to these commercial interests. All other authors declare no competing interests.

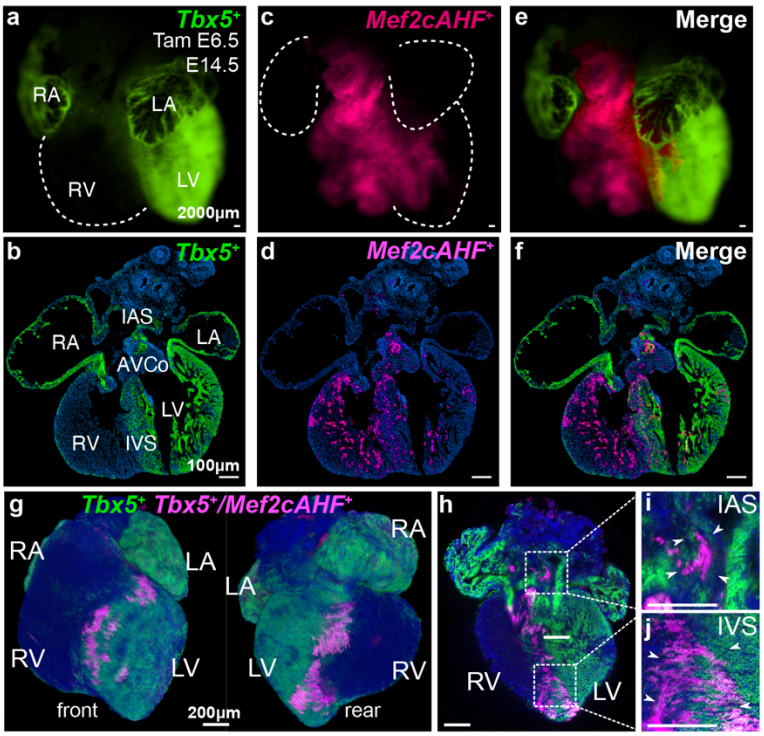

Figure 1. *Tbx5⁺/Mef2cAHF⁺* lineage marks a compartment boundary at the cardiac interventricular septum (IVS). a, **b**, At E14.5, clonal cell descendants of a *Tbx5⁺* lineage (ZsGreen) labeled at E6.5 contributes to the LV. **c**, **d**, a *Mef2cAHF⁺* lineage (tdTomato immunostaining) contributes to the RV, demonstrating largely complementary patterns. **e**, These lineages overlap (*Tbx5⁺/Mef2cAHF⁺*) at the IVS, as well as the atrioventricular complex (AVCo) region, and inter-atrial septum (IAS). *Tbx5*$^{CreERT2/+}$;*Mef2cAHF-DreERT2*;*ROSA26*$^{Ai6/Ai66b}$ hearts by epifluorescence microscopy (a, c, e; scale bars: 200 microns) and cryosections (b, d, f; scale bars: 100 microns). **g-j**, Maximal projection images by lightsheet microscopy of an intersectional reporter for the *Tbx5⁺/Mef2cAHF⁺* lineage (tdTomato immunostaining) in *Tbx5*$^{CreERT2/+}$;*Mef2cAHF-DreERT2*;*ROSA26*$^{Ai66/+}$ embryos at E14.5. Scale bars: 200 microns.

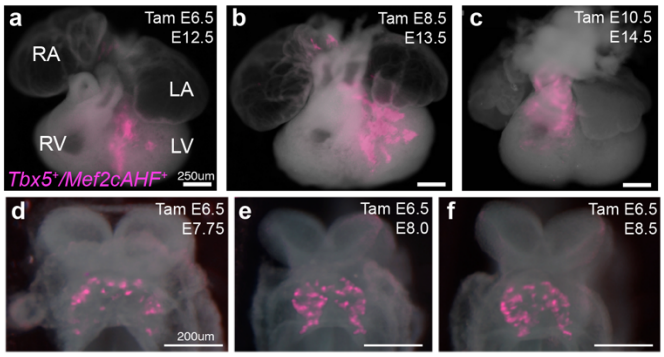

Extended Data Figure 1. a-c, *Tbx5*$^{+}$*/Mef2cAHF*$^{+}$ lineage contributions to the interventricular septum were descendants from progenitors labeled at (a) E6.5, but not at (b) E8.5 or (c) E10.5 in *Tbx5*$^{CreERT2/+}$;*Mef2cAHF-DreERT2*;*ROSA26*$^{Ai6/Ai66}$ embryos. Scale bars: 250 microns. **d-e**, Epifluorescence microscopy images of the *Tbx5*$^{+}$*/Mef2cAHF*$^{+}$ lineage (tdTomato immunostaining) labeled by a single dose of tamoxifen at E6.5 of embryos at (d) E7.75, (e) E8.0 and (f) E8.5 displayed an apparent “salt and pepper” pattern in the early developing heart. Scale bars: 200 microns.

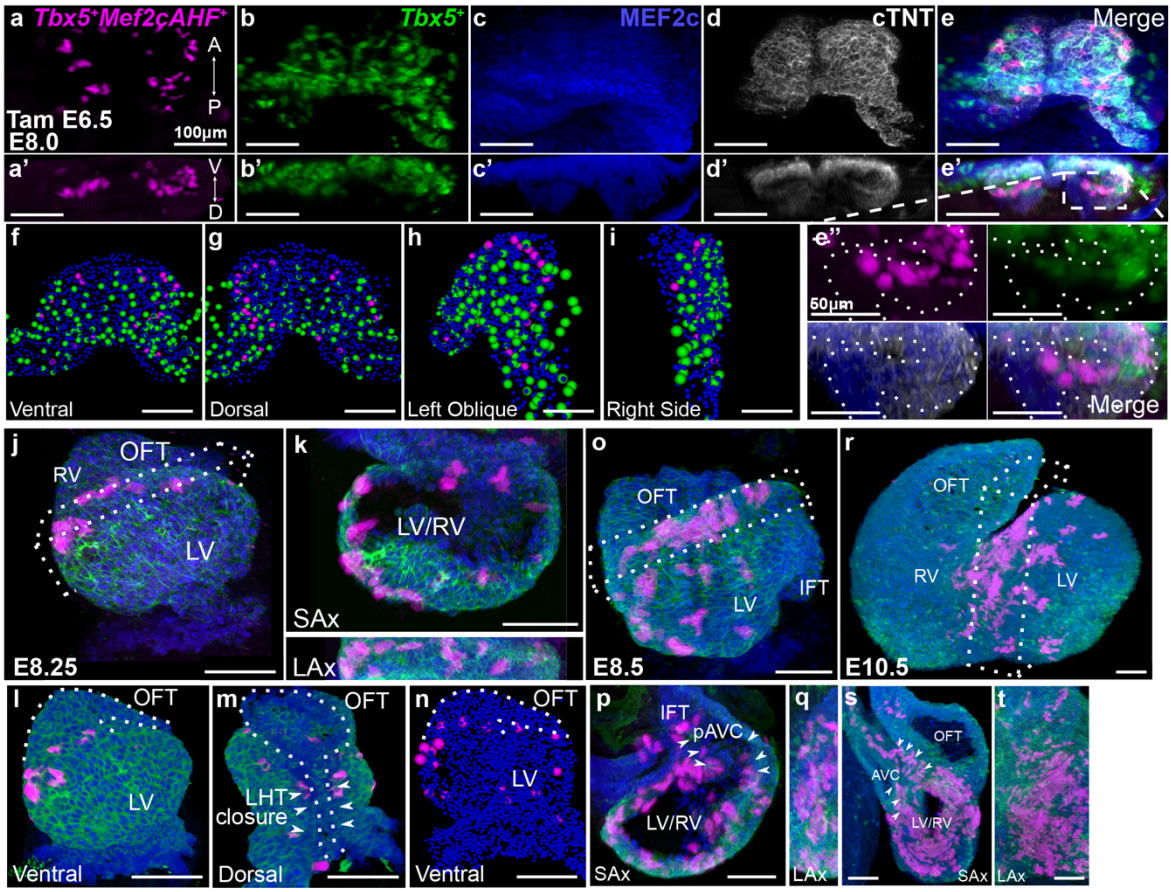

Figure 2. *Tbx5⁺/Mef2cAHF⁺* lineage is prefigured in early mouse heart development. a-i, Frontal (a-e), transverse (a'-e'), magnified transverse (e''), and (f-i) cell segmentation views of maximum Z-projections of whole mount embryos by lightsheet imaging at E8.0 show the *Tbx5⁺* lineage (ZsGreen), and immunostaining of tdTomato for the *Tbx5⁺/Mef2cAHF⁺* lineage, MEF2c and cardiac troponin T (cTNT) in *Tbx5*$^{CreERT2/+}$;*Mef2cAHF-DreERT2*;*ROSA26*$^{Ai6/Ai66}$ embryos. A-P, anterior-posterior axis; V-D, ventral-dorsal axis. At E8.0 (approximately 3 somites), *Tbx5⁺* lineage cells are restricted to a ventral domain, whereas *Tbx5⁺/Mef2cAHF⁺* lineage cells originate along a boundary separating presumptive *Tbx5⁺* and *Tbx5⁻*-lineage compartments. *Tbx5⁺/Mef2cAHF⁺* lineage cells lie in an apparent planar ringlet in the dorsal-ventral axis that expands as the heart tube grows. **j-n**, At E8.25 (approximately 6 somites), with dorsal closure of the linear heart tube (LHT) underway, the *Tbx5⁺/Mef2cAHF⁺* lineage cells form a ring situated between the RV and LV primordia, which is observed from multiple perspectives including anterior, short-axis (SAx) and long-axis (LAx) views. **o-q**, At E8.5 (approximately 9 somites), *Tbx5⁺/Mef2cAHF⁺* lineage cells are observed in a portion of the AV canal primoridium (pAVC and arrowheads). **r-t**, At E10.5, a band of *Tbx5⁺/Mef2cAHF⁺* lineage cells extends from the interventricular groove at the outer curvature to the inner curvature of the heart. SAx and LAx show that *Tbx5⁺/Mef2cAHF⁺* lineage cells occupies a crossroads for heart morphogenesis, spanning the growing interventricular septum to the AV canal (AVC), adjacent to the OFT. All scale bars equal 100 microns.

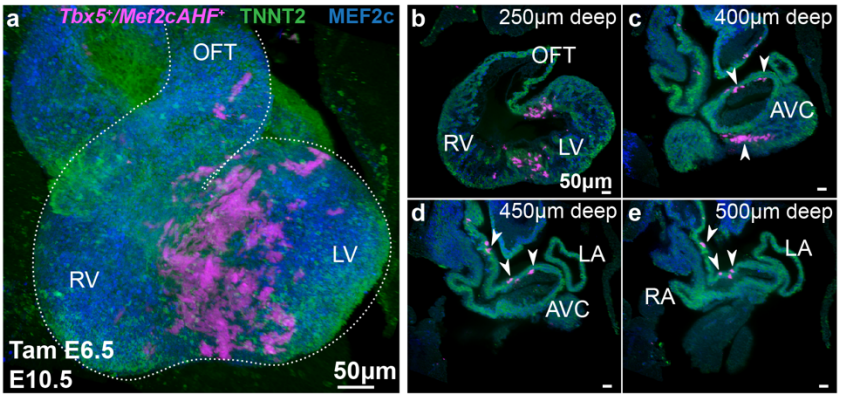

Supplementary Figure 1. *Tbx5⁺/Mef2cAHF⁺* lineage contributions to the developing atria. **a-e**, In the developing atria at E10.5, optical sections from ventral to dorsal show lineage-labeled *Tbx5⁺/Mef2cAHF⁺* lineage cells marked at E6.5 by a single tamoxifen dose is located from the AV canal (AVC) region to the roof of the atrium, prior to the formation of the interatrial septum, in *Tbx5*$^{CreERT2/+}$;*Mef2cAHF-DreERT2*;*ROSA26*$^{Ai6/Ai66}$ embryos. All scale bars equal 50 microns.

Video 1. Related to Figure 2 and Supplemental Figure 1.

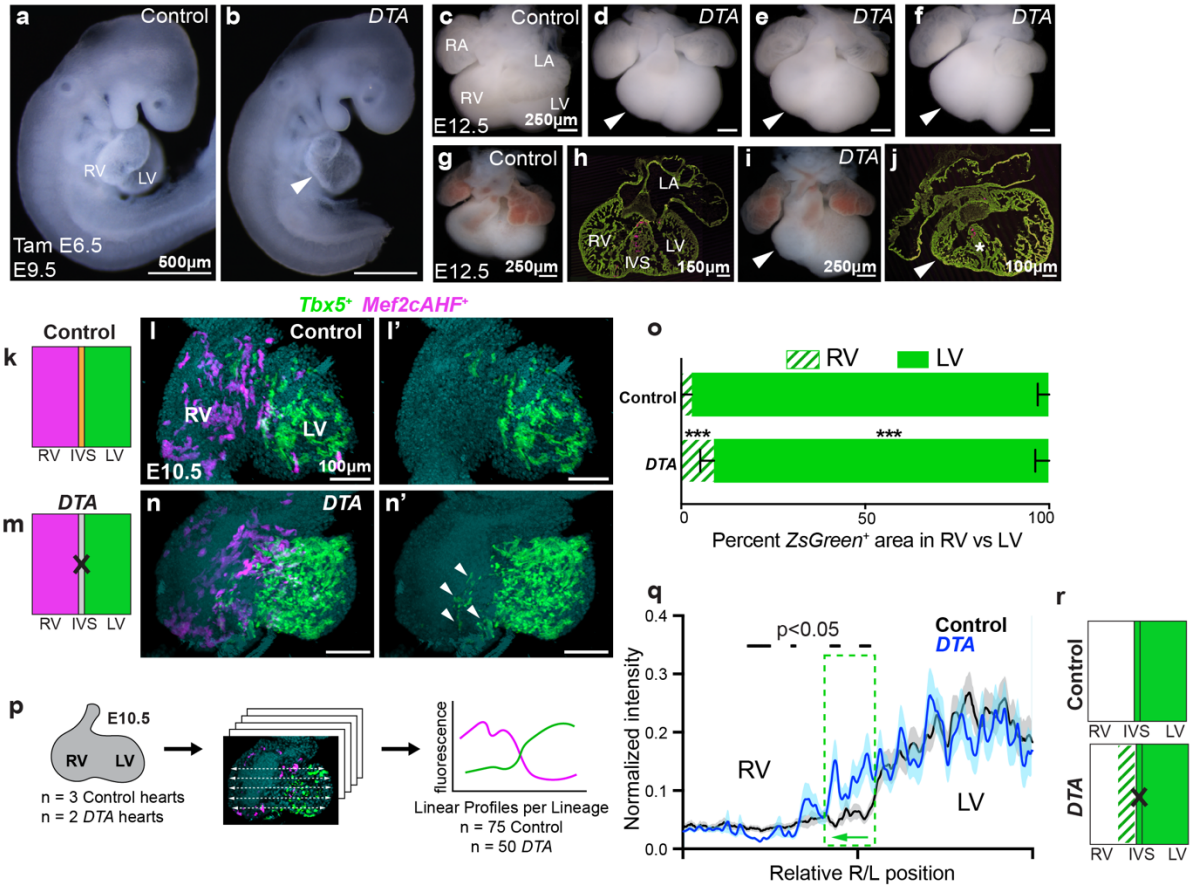

Figure 3. Cell ablation of *Tbx5*⁺/*Mef2cAHF*⁺ progenitors causes RV hypoplasia, IVS disorganization, and lineage mixing. a-j, Misexpression of *diphtheria toxin* (*DTA*) in *Tbx5*⁺/*Mef2cAHF*⁺ progenitors in *Tbx5*$^{CreERT2/+}$;*Mef2cAHF-DreERT2*;*ROSA26*$^{Ai66/+}$;*Hip11*$^{intersectional\text{-}DTA/+}$ embryos (*DTA*), compared to *Tbx5*$^{CreERT2/+}$;*Mef2cAHF-DreERT2*;*ROSA26*$^{Ai66/+}$;*Hip11*$^{+/+}$ (control), resulted in right ventricle (RV) hypoplasia (arrows) at E9.5 (a, b; scale bars: 500 microns), and E12.5 (c-j; scale bars 250 microns), along with disorganization and non-compaction of the interventricular septum (IVS) (asterisk) (g-j). right atrium (RA), left atrium (LA). **k-n'**, At E10.5, mixing of *Tbx5*⁺ lineage (white arrows in n' show ectopic *Tbx5*⁺ lineage ZsGreen cell in the right heart) was observed by lightsheet microscopy in *Tbx5*$^{CreERT2/+}$;*Mef2cAHF-DreERT2*;*ROSA26*$^{Ai6/Ai66b}$;*Hip11*$^{intersectional\text{-}DTA/+}$ embryos (*DTA*) (n=2) compared to *Tbx5*$^{CreERT2/+}$;*Mef2cAHF-DreERT2*;*ROSA26*$^{Ai6/Ai66b}$;*Hip11*$^{+/+}$ embryos (control) (n=3). (k, m) Cartoon depictions of experiment. **o**, Distribution of the *Tbx5*⁺ lineage by ventricular chamber demonstrates that the *Tbx5*⁺ lineage is increased in the RV of *DTA* mutants (p=0.000513 by two-sided T test), compared to controls. Cells of the RV and left ventricle (LV) were evaluated in five optical slices at different anterior-posterior planes per embryonic heart sample of 3 controls and 2 mutants. Mean and standard deviation are shown. **p-r**, Linear profiles quantified fluorescence intensity across the heart at the right or left (R/L) positions. *Tbx5*⁺ lineage cells expanded rightward into the RV (depiction in (r) by hashed area, dashed green box in (q) shows significant difference between traces, indicative of a rightward expansion (green arrow)), consistent with a compartment boundary disruption. Linear profiles at 5 apical-basal planes per optical slice, for 5 optical slices at different anterior-posterior planes per embryonic heart sample of 3 controls and 2 *DTA* mutants were assessed, as depicted in (p). Statistical significance (p<0.05) between linear profiles of control and *DTA* mutants was determined by Welch's two-sided t-test at each position

912 along the right-left axis. Mean and standard error of the mean are shown. Precise p-values can
913 be found in the Source data.
914

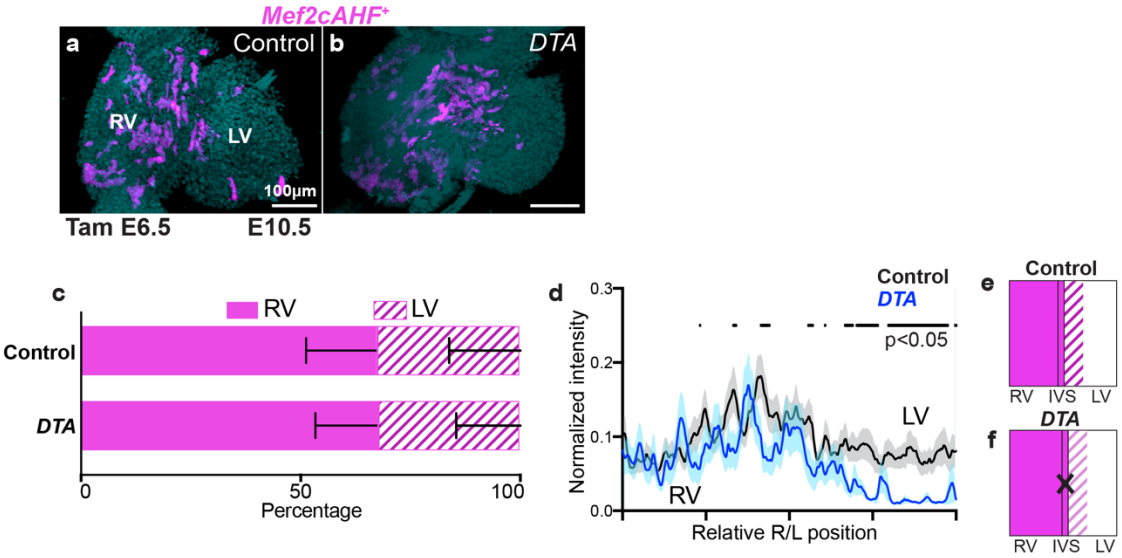

Extended Data Figure 2. *Mef2cAHF*+ lineage distribution in intersectional-*DTA* mutants. a, *Mef2cAHF*+ lineage was enriched in the RV of control embryos (*Tbx5*$^{CreERT2/+}$*;Mef2cAHF-DreERT2;Hip11*$^{+/+}$) (n=3) and (**b**) intersectional-*DTA* mutant embryos (*Tbx5*$^{CreERT2/+}$*;Mef2cAHF-DreERT2;Hip11*$^{Intersectional\text{-}DTA176/+}$) (n=2). **c**, This distribution of the *Mef2cAHF*+ lineage was not different in the RV or LV between control and *DTA* mutants (p=0.939327, by two-sided T-test). Cells of the right ventricle (RV) or left ventricle (LV) in five optical slices at different anterior-posterior planes per embryonic heart sample of 3 controls and 2 mutants were evaluated. Mean and standard deviation are shown. **d**, Linear profiles showed a reduction of fluorescence activity in the LV. Linear profiles at 5 apical-basal planes per optical slice, for 5 optical slices at different anterior-posterior planes per embryonic heart sample of 3 controls and 2 *DTA* mutants were assessed. Statistical significance (p<0.05) between linear profiles of control and *DTA* mutants was determined by Welch's two-sided t-test at each position along the right-left axis. Mean and standard error of the mean are shown. Precise p-values can be found in the Source data. **e, f**, Cartoon depictions.

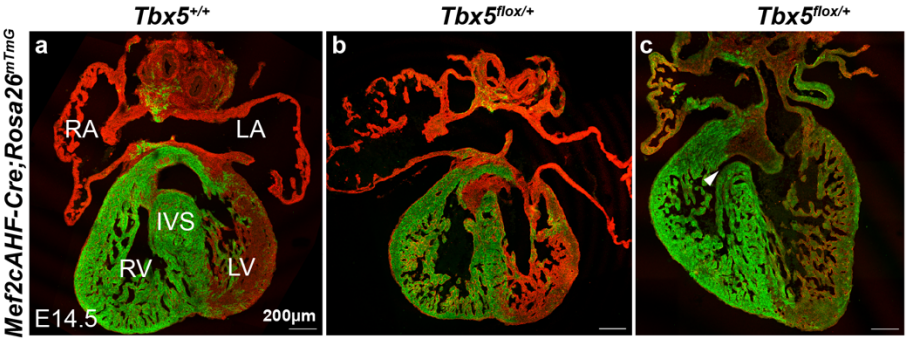

Extended Data Figure 3. Conditional haploinsufficiency of *Tbx5* in the interventricular septum (IVS) leads to ventricular septal defects (VSDs). a-c, At E14.5, membranous VSDs were observed in *Mef2cAHF-Cre*;*ROSA26*$^{mTmG/+}$;*Tbx5*$^{flox/+}$ mutant embryos (n=4/7) compared to *Mef2cAHF-Cre*;*ROSA26*$^{mTmG/+}$;*Tbx5*$^{flox/+}$ controls (n=0/3). Right ventricle (RV), left ventricle (LV) and interventricular septum (IVS). All scale bars equal 200 microns.

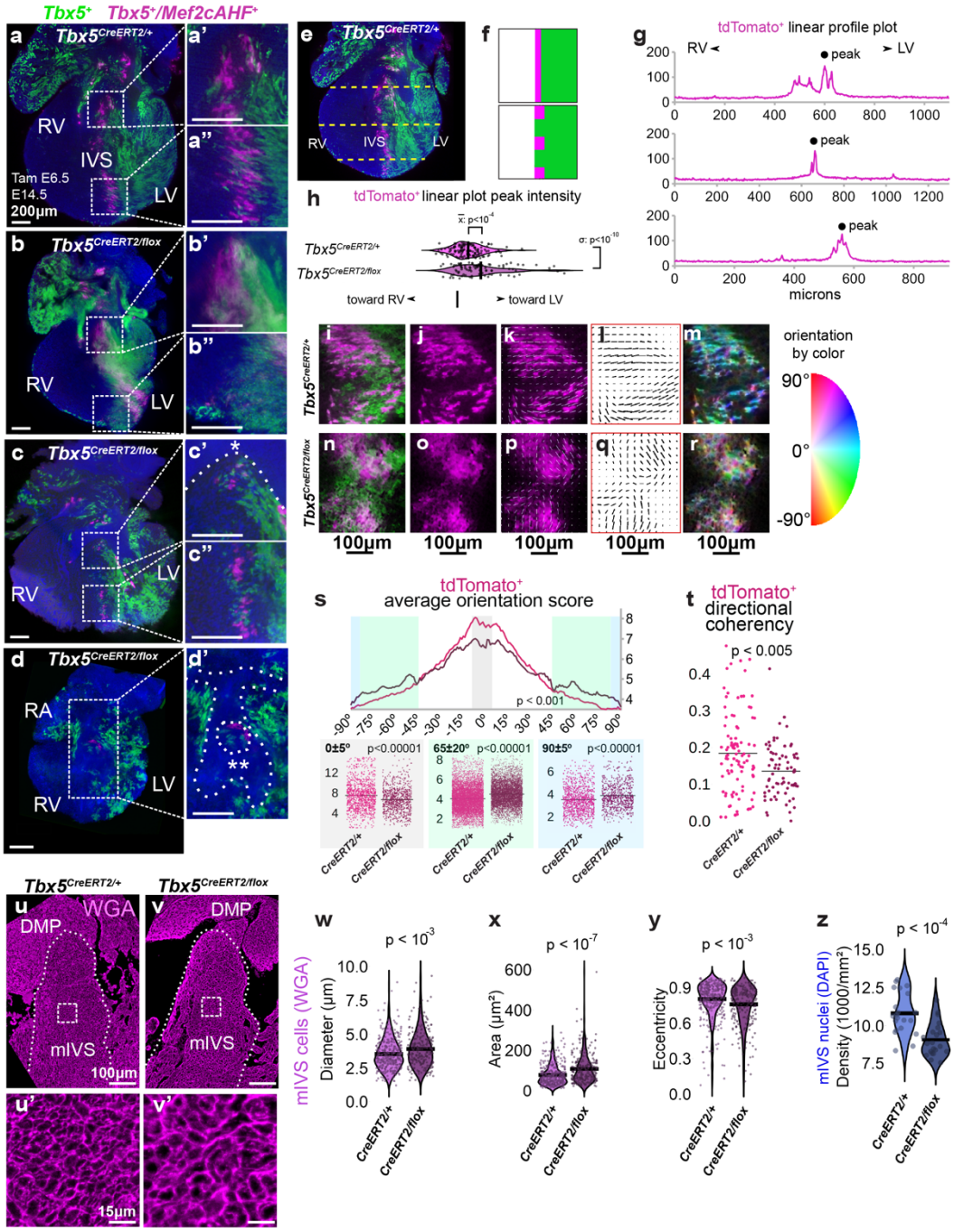

Figure 4. Reduced TBX5 dosage caused ventricular septal defects (VSDs), perturbations to IVS boundary position and integrity, and abnormal IVS cell arrangement. a, Mid-posterior optical sections from lightsheet microscopy of a control (*Tbx5*$^{CreERT2/+}$;*Mef2cAHF-DreERT2*;*ROSA26*$^{Ai6/Ai66}$) heart display *Tbx5*$^{+}$ lineage (ZsGreen) and *Tbx5*$^{+}$*/Mef2cAHF*$^{+}$ lineage (tdTomato immunostaining) cells. *Tbx5*$^{+}$*/Mef2cAHF*$^{+}$ lineage cells in the interventricular septum (IVS) extended from the base (a') to the apex (a") of the heart, where cells were highly organized. (B-D) A spectrum of phenotypes of *Tbx5*$^{CreERT2/flox}$ mutants (*Tbx5*$^{CreERT2/flox}$*;Mef2cAHF-DreERT2*;*ROSA26*$^{Ai6/Ai66}$) were observed, including intact IVS (b-b"), membranous VSD (c-c", asterisk) and atrioventricular septal defect (double asterisk in d'). **b', b", c', c", d'**, A

maldistribution and disorientation of *Tbx5*$^{+}$/*Mef2cAHF*$^{+}$ lineage cells were observed in *Tbx5*$^{CreERT2/flox}$ mutants. (a-d') sale bars: 200um. **e-h**, Linear plot profiles at positions along the anterior-posterior and apical-middle-basal axis (dashed lines) of control (116 profiles from 4 samples) and *Tbx5*$^{CreERT2/flox}$ mutant (87 profiles from 3 samples) hearts for *Tbx5*$^{+}$/*Mef2cAHF*$^{+}$ lineage cells showed a leftward shift of boundary positioning and broadening of the *Tbx5*$^{+}$/*Mef2cAHF*$^{+}$ lineage position, consistent with lineage mixing. The image in (e) is a repeat of the image in (a). **f**, Cartoon depiction. **g**, Examples of linear profile plots are shown, and (**h**) aggregated data is depicted and quantified. Statistics determined by two-sided unpaired F-test to compare variance (p=2.621e-11) and two-sided unpaired t-test (p=9.741e-05) to compare means. **i-s**, Orientation scores for cells from each channel (tdTomato^{+} or ZsGreen^{+}) was delineated for each genotype, and distributions were plotted as a function of angle. *Tbx5*$^{CreERT2/flox}$ mutant hearts scored worse for orientation of *Tbx5*$^{+}$/*Mef2cAHF*$^{+}$ lineage (tdTomato^{+}) cells in the dominant direction (range from -5 to 5 degrees) and scored higher in the orientation orthogonal to the dominant direction (range from 85 to 95 degrees and -85 to -95 degrees), as determined in (s) by two-sided Watson U2 test across all orientations ($p<0.001$) or by two-sided Wilcoxon rank sum test with continuity correction for selected orientations (p=3.207e-10, 2.2e-16, 7.839e-09, for left-to-right plots). (i-r) scale bars: 100 microns. **t**, *Tbx5*$^{+}$/*Mef2cAHF*$^{+}$ lineage (tdTomato^{+}) cells demonstrated worse directional coherency scoring in *Tbx5*$^{CreERT2/flox}$ mutants (99 regions from 4 controls, 74 regions from 3 mutants) by two-sided Wilcoxon rank sum test with continuity correction (p=0.003845). **u-y**, Cell morphometry at E14.5 by wheat germ agglutinin (WGA) staining of cell membranes in the muscular IVS (mIVS) (dashed outline) of controls (3 planes per sample, 2 samples) and *Tbx5* mutants (3 planes per sample, 2 samples). scale bars: 100 microns (u, v); 15 microns (u', v'). Images of (u-v') are repeated in Supplemental Data Figure 3b, b', f, f'. Quantification of cell (**w**) diameter, (**x**) area, and (**y**) eccentricity. **z**, Nuclei density by DAPI staining of the IVS. Statistics determined by two-sided unpaired T-tests (W: p=0.0002955, X: p=2.9e-08, Y: p=0.0007001, Z: p=5.296e-05).

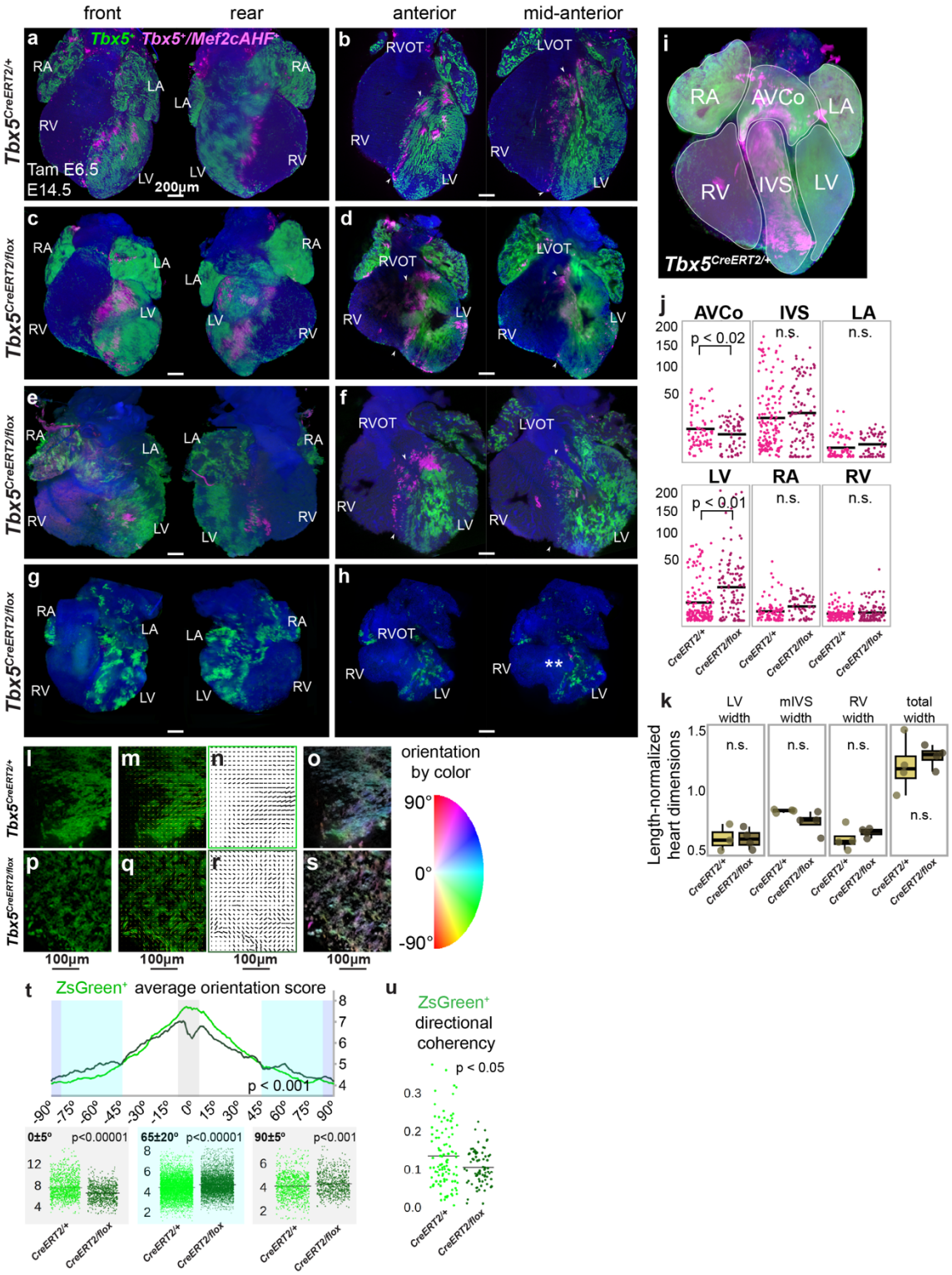

Extended Data Figure 4. Additional samples of *Tbx5* mutant hearts and supplementary quantification of distribution and cell arrangement. a-h, Volume renderings from lightsheet microscopy of anterior and posterior surfaces, as well as anterior and mid-anterior 4-chamber optical sections of *Tbx5*$^{CreERT2/+}$ control (*Tbx5*$^{CreERT2/+}$;*Mef2cAHF-DreERT2*;*ROSA26*$^{Ai6/Ai66}$) and *Tbx5*$^{CreERT2/flox}$ mutant (*Tbx5*$^{CreERT2/flox}$;*Mef2cAHF-DreERT2*;*ROSA26*$^{Ai6/Ai66}$) hearts at E14.5 display

983 *Tbx5*$^{+}$ lineage (ZsGreen) and *Tbx5*$^{+}$*/Mef2cAHF*$^{+}$ lineage (tdTomato immunostaining) cells. (a-h)
984 scale bars: 200 microns. **i-k**, Quantification of the anatomical location of tdTomato^{+} and ZsGreen^{+}
985 cells in *Tbx5*$^{CreERT2/flox}$ mutants (n=3) and *Tbx5*$^{CreERT2/+}$ controls (n=4), by region at E14.5 as
986 outlined in (i). Over 1200 3-dimensional regions of interest were drawn blinded, and then
987 integrated fluorescence signal was assessed. **j**, Although no regional differences in the intensities
988 of ZsGreen^{+} were detected, tdTomato^{+} displayed higher integrated fluorescence in the left
989 ventricle (LV) and less signal in atrioventricular complex (AVCo) complex region by two-sided
990 unpaired T-tests (AVCo: p=0.01933, interventricular septum (IVS): p=0.3679, left atrium (LA):
991 p=0.2829, LV: p=0.0001574, right atrium (RA): p=0.1678, right ventricle (RV): p=0.05063). **k**,
992 Length-normalized widths of LV, muscular IVS (mIVS), RV and total heart at E14.5 were not
993 significantly different between control (n=4) and *Tbx5* mutants (n=3) based on regions of interest
994 in (i), by two-sided unpaired T-tests (p=0.9654, 0.1277, 0.3797, 0.5631 for left-to-right plots).
995 Median, first and third quartiles are shown in box plots. Further details are in Source data. **l-u**,
996 *Tbx5*$^{CreERT2/flox}$ mutant hearts at E14.5 scored worse for orientation scores of *Tbx5*$^{+}$ lineage
997 (ZsGreen^{+}) cells in the dominant direction (range from -5 to 5 degrees) and scored higher in the
998 orientation orthogonal to the dominant direction (range from 85 to 95 degrees and -85 to -95
999 degrees), as determined (**t**) by two-sided Watson U2 test across all orientations (p<0.001) or by
1000 two-sided Wilcoxon rank sum test with continuity correction for selected orientations (p-values <
1001 2.2e-16 for left and middle plots, p-value = 0.0006863 for right plots). **u**, *Tbx5*$^{+}$ lineage (ZsGreen^{+})
1002 cells demonstrated worse directional coherency scoring in *Tbx5*$^{CreERT2/flox}$ mutants by two-sided
1003 Wilcoxon rank sum test with continuity correction (p=0.03316). (l-s) scale bars are 100 microns.
1004
1005 **Video 2.** Related to Figure 4 and Extended Data Figure 4.
1006
1007
1008

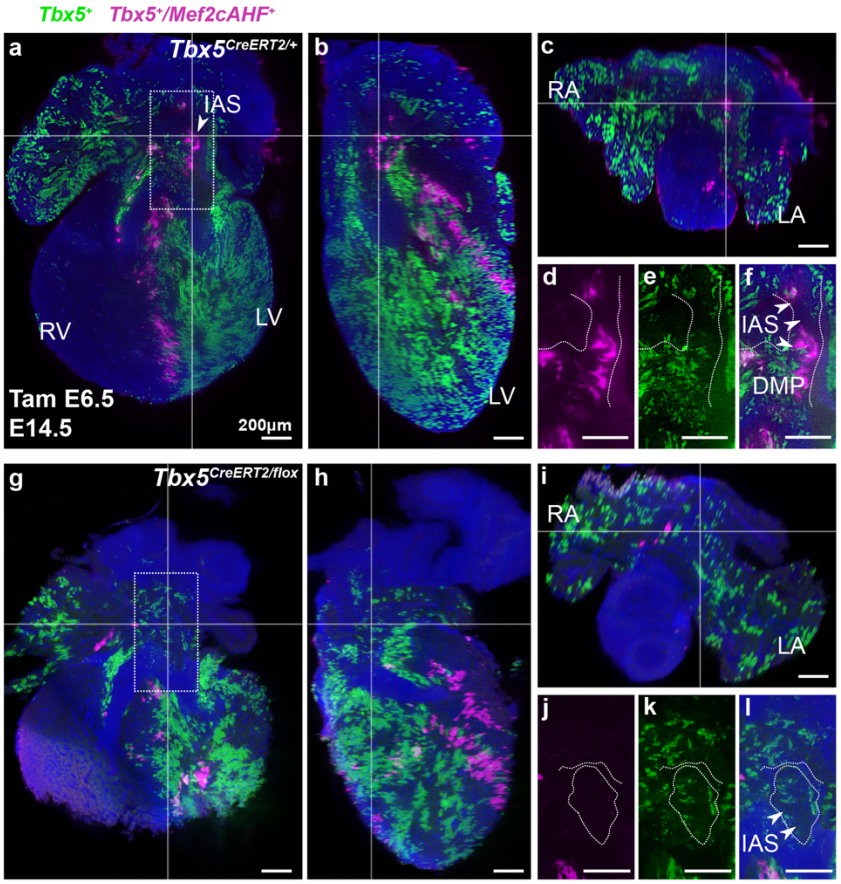

Supplemental Figure 2. Reduced TBX5 dosage leads to reduced contributions of the *Tbx5⁺/Mef2cAHF⁺* lineage to the inter-atrial septum and dorsal mesenchymal protrusion. a-f, At E14.5, the *Tbx5⁺*/*Mef2cAHF⁺* lineage cells contribute to the interatrial septum (IAS, arrowheads) and dorsal mesenchymal protrusion (DMP) in *Tbx5*$^{CreERT2/+}$ controls (*Tbx5*$^{CreERT2/+}$;*Mef2cAHF-DreERT2*;*ROSA26*$^{Ai6/Ai66}$). **g-l**, The *Tbx5⁺*/*Mef2cAHF⁺* lineage cells are less apparent in *Tbx5* mutants (*Tbx5*$^{CreERT2/flox}$;*Mef2cAHF-DreERT2*;*ROSA26*$^{Ai6/Ai66}$). Right ventricle (RV), left ventricle (LV), right atrium (RA), left atrium (LA). All scale bars equal 200 microns.

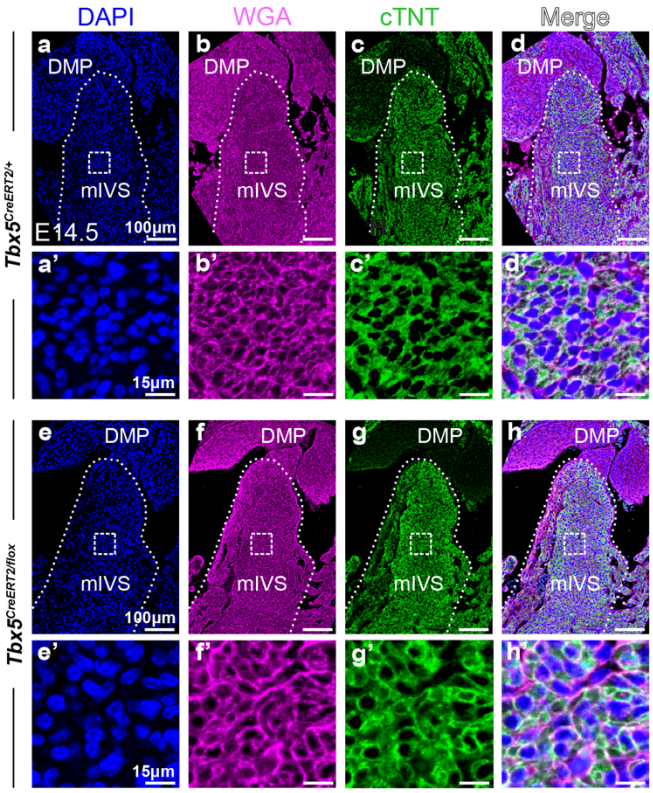

Supplemental Figure 3. Images for quantification of cell geometry, and assessment of tissue architecture in *Tbx5* mutants. a-d', *Tbx5*$^{CreERT2/+}$ control (*Tbx5*$^{CreERT2/+}$;*Mef2cAHF-DreERT2*;*ROSA26*$^{Ai6/Ai66}$) (3 planes per sample, 2 samples) and (**e-h'**) *Tbx5*$^{CreERT2/flox}$ mutant (*Tbx5*$^{CreERT2/flox}$;*Mef2cAHF-DreERT2*;*ROSA26*$^{Ai6/Ai66}$) hearts (3 planes per sample, 2 samples) after single dose of tamoxifen injected at E6.5 is shown at E14.5, stained with DAPI, wheat germ agglutinin (WGA), or cardiac troponin T (cTNT). (b, b', f, f') are repeat images of Figure 4u-v'. scale bars: 100 microns (a-h); 15 microns (a'-h').

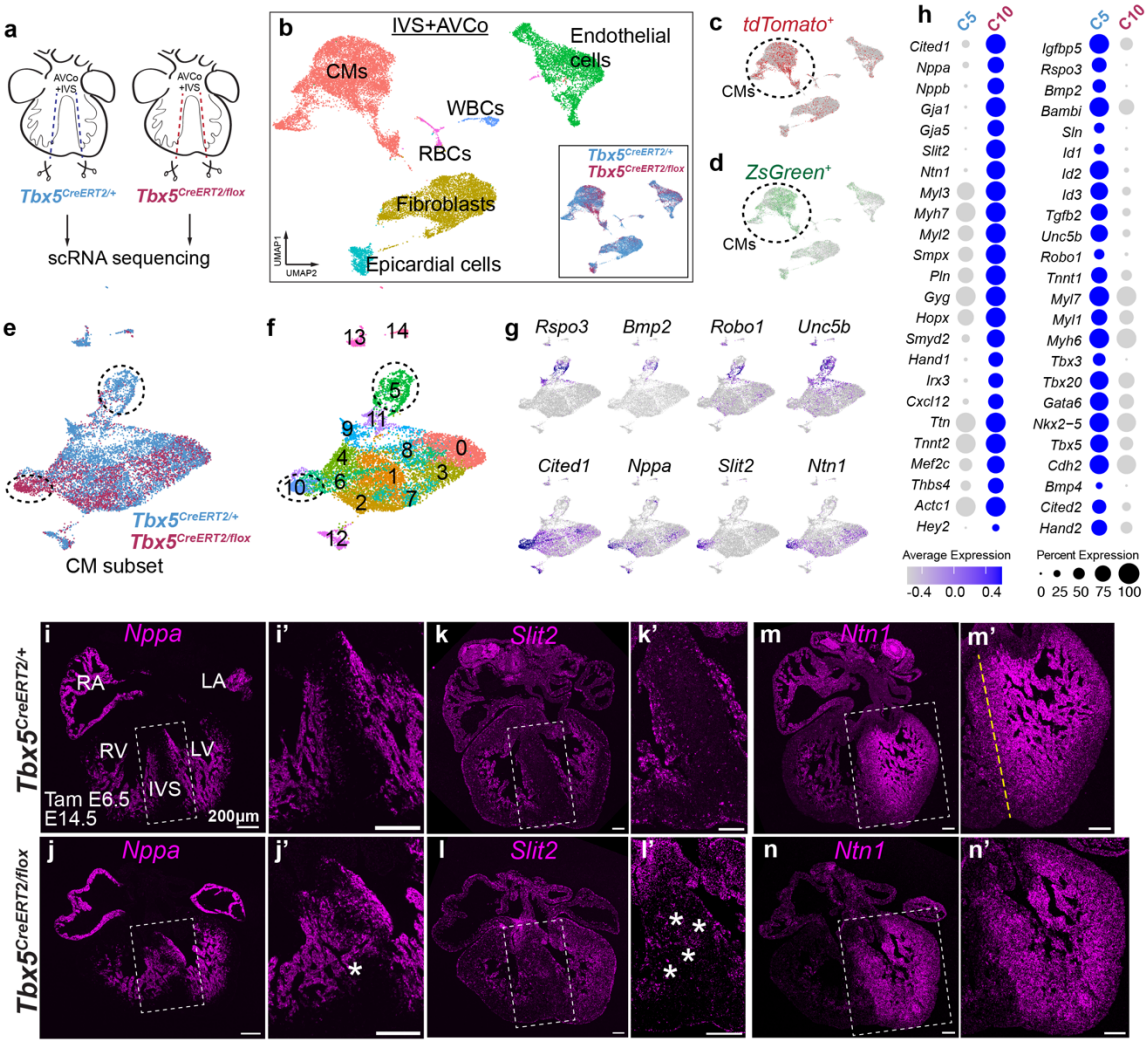

Figure 5. *Slit2* and *Ntn1* are *Tbx5*-sensitive genes in the interventricular septum (IVS). a, At E13.5, we micro-dissected the right ventricle (RV), left ventricle (LV) and IVS+atrioventricular complex (AVCo) regions in *Tbx5*$^{CreERT2/+}$ controls and *Tbx5*$^{CreERT/flox}$ mutants (*Tbx5*$^{CreERT2/flox}$*;Mef2cAHF-DreERT2;ROSA26*$^{Ai6/Ai66}$) with the labeled *Tbx5*$^{+}$*/Mef2cAHF*$^{+}$ lineage (*tdTomato*$^{+}$) and *Tbx5*$^{+}$ lineage (*ZsGreen*$^{+}$) cells, after a single dose of tamoxifen at E6.5. **b**, UMAP visualization of IVS+AVCo by cell type clusters and *Tbx5* genotype (inset) (controls, n=4; *Tbx5* mutants, n=2). CMs, cardiomyocytes; WBCs, white blood cells; RBCs, red blood cells. **c**, *ZsGreen*$^{+}$ and (**d**) *tdTomato*$^{+}$ cells are enriched among CMs. **e**, UMAP shows a *Tnnt2*$^{+}$ CM subset by *Tbx5* genotype or (**f**) Louvain clusters. **g**, Feature plots show that AVCo region genes (*Rspo3, Bmp2, Robo1, Unc5b*) are enriched among control-enriched cluster 5, suggesting downregulation of these genes in *Tbx5* mutants. Trabecular genes (*Cited1, Nppa, Slit2, Ntn1*) were enriched in the *Tbx5* mutant-enriched cluster 10. **h**, Dot plots of selected genes that are upregulated in cluster 10 (C10) or in cluster 5 (C5). Significance of adj $p<0.05$ was determined by two-sided Wilcoxan rank sum. **i-n**, Fluorescent *in situ* hybridization of trabecular genes *Nppa*, *Slit2* and *Ntn1* in *Tbx5*$^{CreERT2/+}$ controls or *Tbx5*$^{CreERT2/flox}$ mutants at E14.5. **i, i', k, k'**, *Nppa* and *Slit2* are normally expressed in the ventricular trabecular layer and excluded from the core of the IVS. **j, j', l, l'**, In a *Tbx5*$^{CreERT2/flox}$ mutant with an intact IVS, *Nppa* and *Slit2* are misexpressed in the IVS (asterisks). **m, m'**, *Ntn1* is normally expressed in the trabecular layer and in a gradient across the IVS from

1049 left to right, demarcated by yellow dashed line. **n, n'**, In a *Tbx5*$^{CreERT2/flox}$ mutant with an intact IVS,
1050 *Ntn1* is expanded across the IVS, flattening its gradient. All scale bars equal 200 microns.
1051
1052

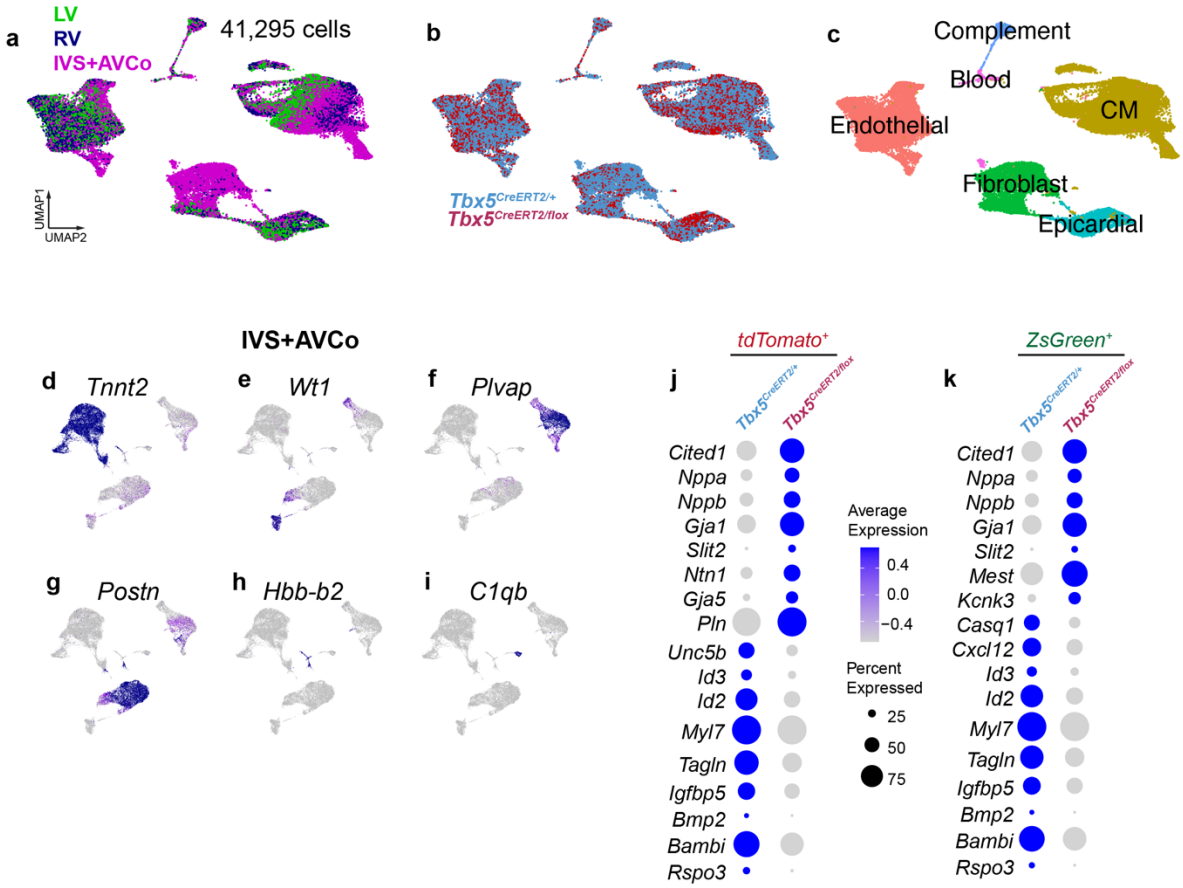

Extended Data Figure 5. scRNA-seq of *Tbx5* mutants by region. a-c, In scRNA-seq samples from E13.5 hearts, we display cells by (**a**) region (left ventricle (LV), right ventricle (RV), interventricular septu (IVS)) (**b**) genotype, or (**c**) cell types by Louvain clustering. In IVS+atrioventricular complex (AVCo) regions (control, n=4, *Tbx5* mutant, n=2), we detected clusters enriched for (**d**) *Tnnt2*+ cardiomyocytes (CMs), (**e**) *Tbx18*+/*Wt1*+ epicardial cells, (**f**) *Plvap*+ endothelial cells, (**g**) *Postn*+ fibroblasts, (**h**) *Hbb-b2*+ red blood cells, and (**i**) *C1qb*+ white blood cells. Dot plots of selected differentially expressed genes in (**j**) *tdTomato*+ or (**k**) *ZsGreen*+ cells from the IVS+AVCo region. Significance of adj $p<0.05$ was determined by two-sided Wilcoxan rank sum.

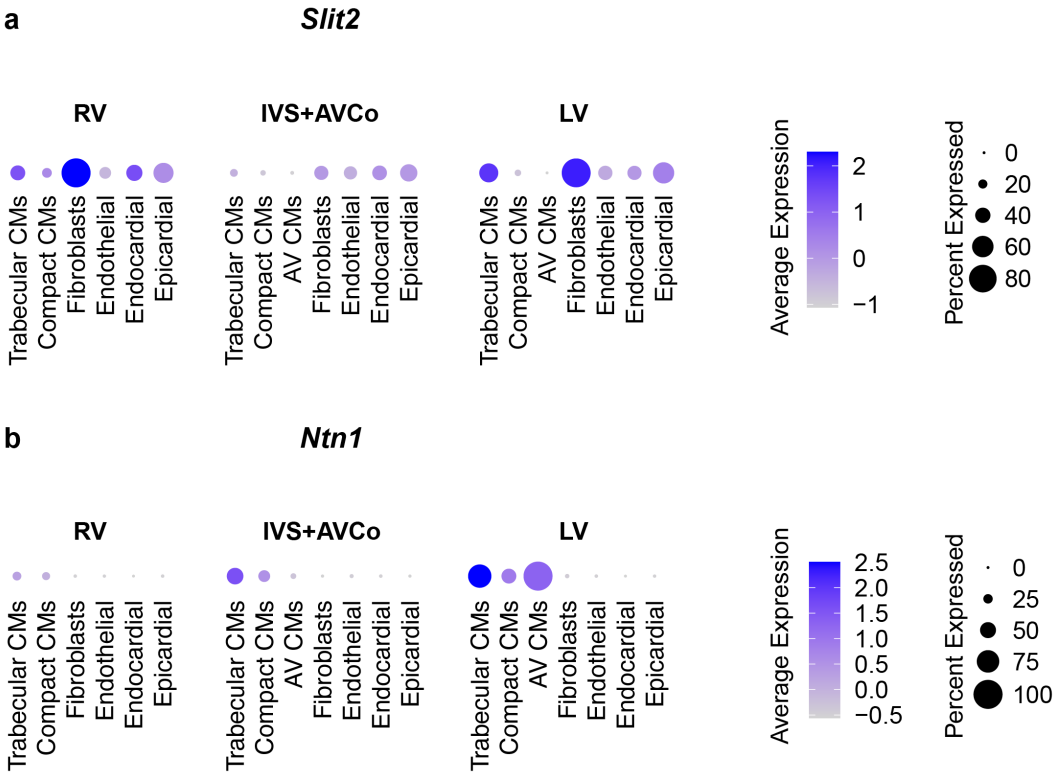

Supplementary Figure 4. Gene expression of *Slit2* and *Ntn1* by cell type in individual cells of the developing heart. By scRNA-seq from control E13.5 hearts (n=4), gene expression of (**a**) *Slit2* and (**b**) *Ntn1* are shown by region (left ventricle (LV), right ventricle (RV), interventricular septum (IVS)+atrioventricular complex (AVCo) regions).

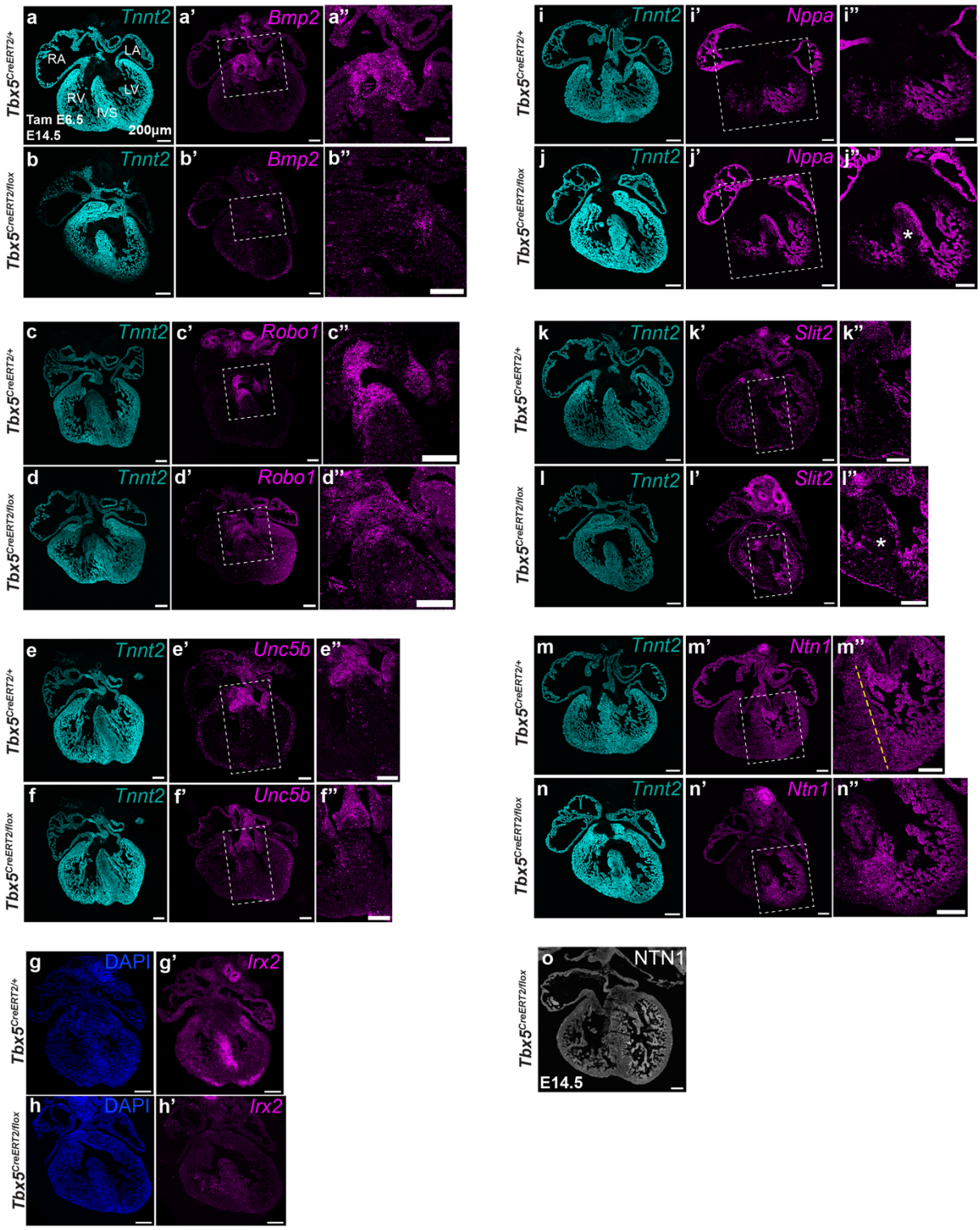

Extended Data Figure 6. Fluorescent *in situ* hybridization of *Tbx5*-dependent genes at E14.5. a-f'', By fluorescent *in situ* hybridization at E14.5 after a single dose of tamoxifen at E6.5, *Bmp2*, *Robo1* and *Unc5b* are expressed in the atrioventricular canal (boxed region) in *Tbx5*$^{CreERT2/+}$ controls (*Tbx5*$^{CreERT2/+}$;*Mef2cAHF-DreERT2*;*ROSA26*$^{Ai6/Ai66}$), and expression of these genes are reduced in *Tbx5*$^{CreERT2/flox}$ mutants (*Tbx5*$^{CreERT2/flox}$;*Mef2cAHF-DreERT2*;*ROSA26*$^{Ai6/Ai66}$).

Tnnt2 is expressed in cardiomyocytes. **g-h'**, *Irx2* is reduced in the IVS of *Tbx5* mutants. **i-n''**, *Nppa*, *Slit2* and *Ntn1* are expressed in the trabecular layer in *Tbx5*$^{CreERT2/+}$ controls, and misexpressed in the IVS in *Tbx5*$^{CreERT2/flox}$ mutants with a membranous VSD at E14.5. Yellow dashed line demarcates gradient of *Ntn1* expression across the IVS from left to right. **o**, Immunostaining of NTN1 at E14.5. All scale bars are 200 microns.

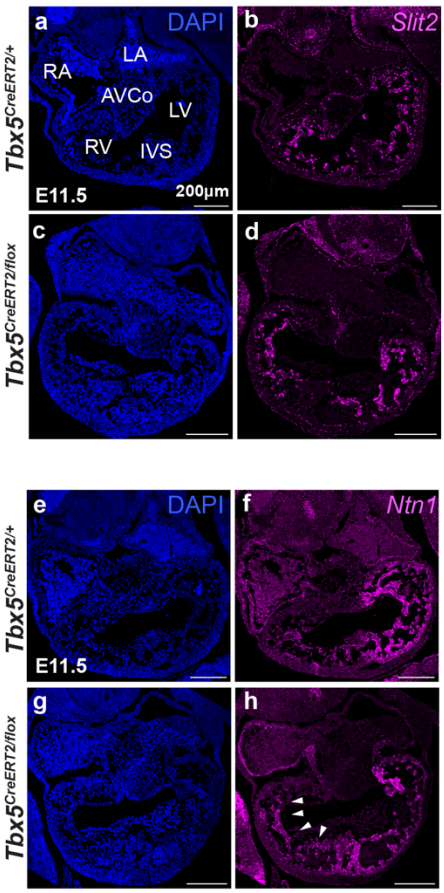

Extended Data Figure 7. Expression of *Slit2* and *Ntn1* in *Tbx5* mutants at E11.5. Fluorescent *in situ* hybridization of (**a-d**) *Slit2* and (**e-h**) *Ntn1* at E11.5 in *Tbx5*$^{CreERT2/+}$ controls (*Tbx5*$^{CreERT2/+}$;*Mef2cAHF-DreERT2*;*ROSA26*$^{Ai6/Ai66}$) and *Tbx5*$^{CreERT2/flox}$ mutant (*Tbx5*$^{CreERT2/flox}$;*Mef2cAHF-DreERT2*;*ROSA26*$^{Ai6/Ai66}$) hearts. Arrowheads highlight ectopic expression of *Ntn1* in the RV. All scale bars are 200 microns.

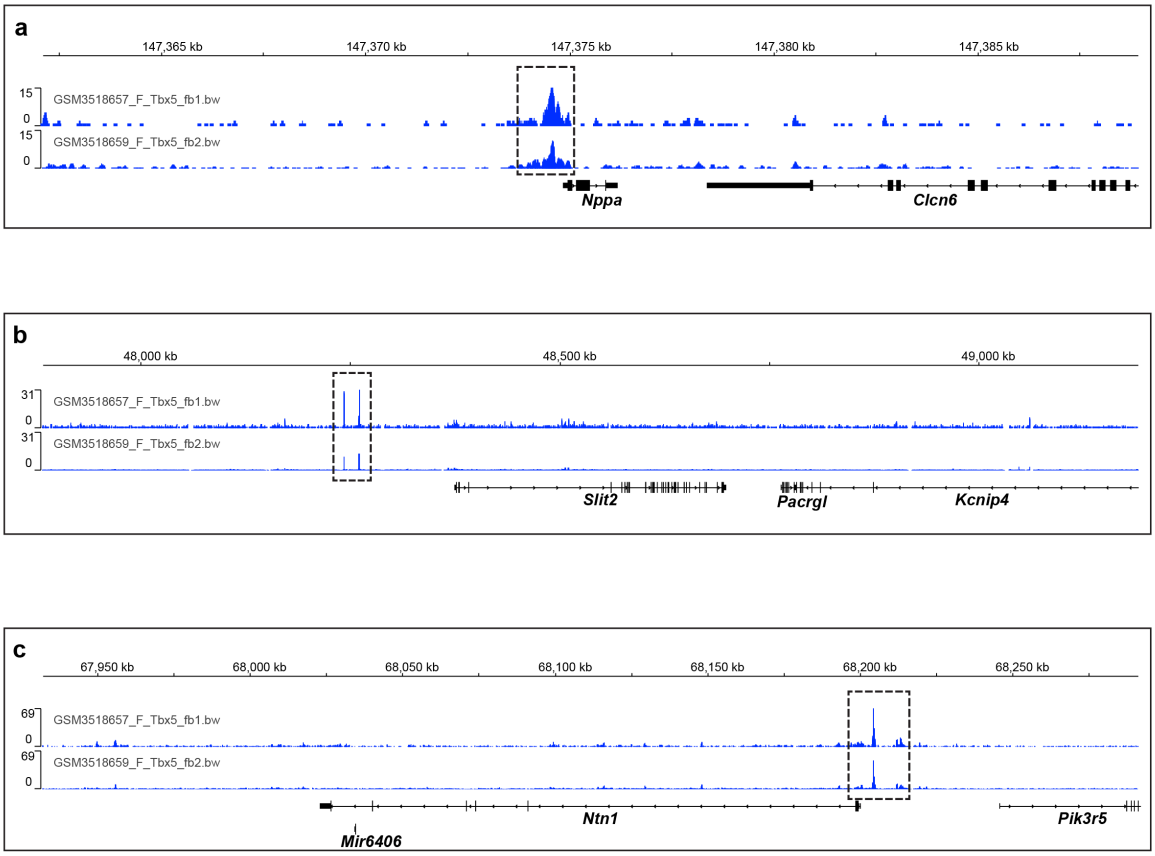

Extended Data Figure 8. TBX5 chromatin occupancy near *Slit2* and *Ntn1*. a-c, Browser tracks of TBX5 ChIP-seq from E12.5 hearts [55] show peaks of TBX5 occupancy (dashed black boxes) near promoters of *Nppa*, *Slit2* and *Ntn1*.

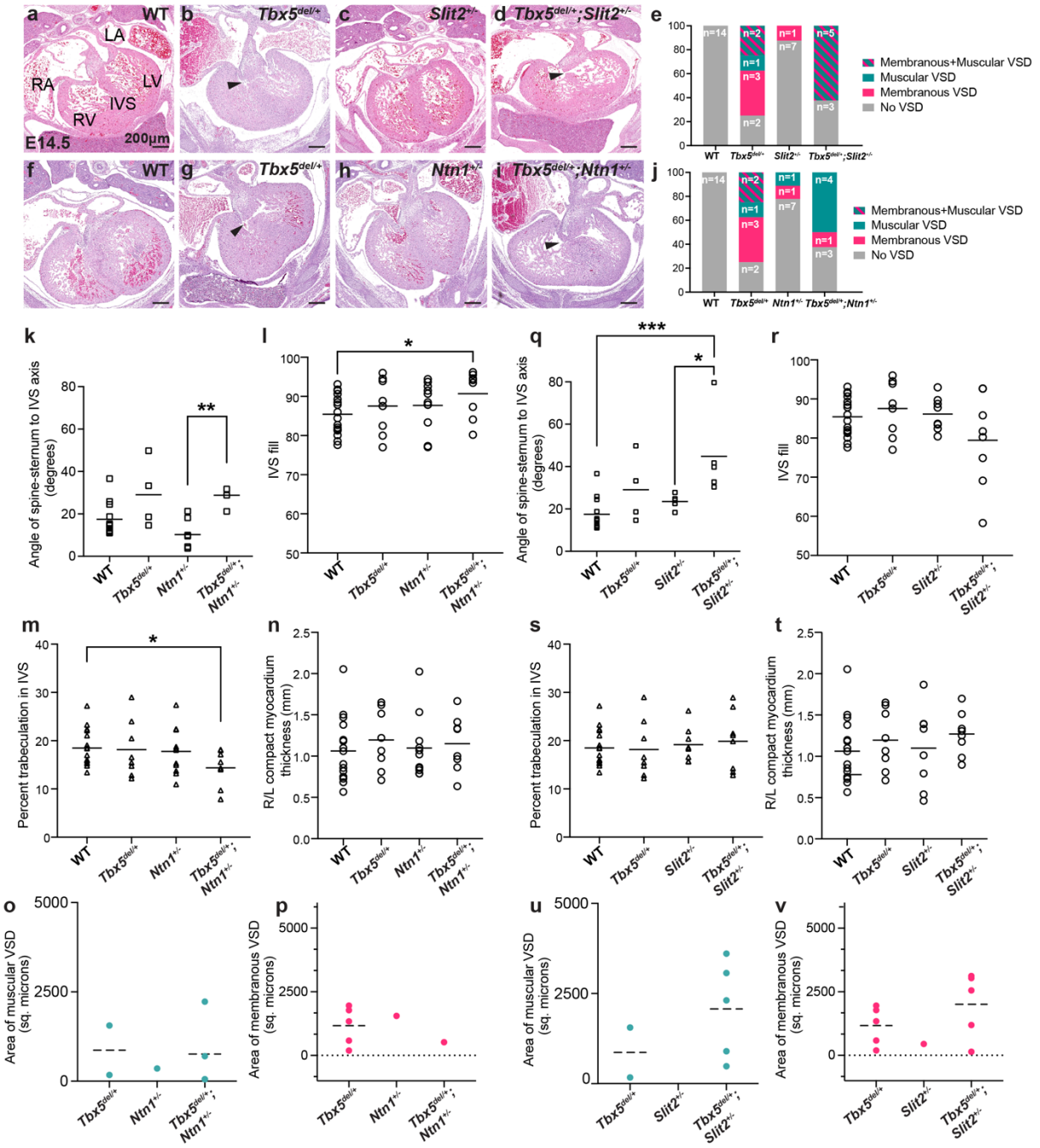

Extended Data Figure 9. *Tbx5-Ntn1* and *Tbx5-Slit2* genetic interactions. Histology from E14.5 embryos from matings of (**a-d**) *Tbx5*$^{del/+}$ and *Slit2*$^{+/-}$ or (**f-i**) *Tbx5*$^{del/+}$ and *Ntn1*$^{+/-}$ by genotype. Arrowheads depict muscular ventricular septal defects (VSDs). **e,** Quantification of membranous or muscular VSDs by genotype. *Tbx5*$^{del/+}$;*Slit2*$^{+/-}$compound heterozygous embryos displayed an estimated decrease in the incidence of membranous VSDs, which approached significance (log OR -2.5; p=0.09 in a Generalized Linear Model without adjustments for multiple comparisons). This decrease was relative to the expected incidence of membranous VSDs if there was no genetic interaction between *Tbx5* and *Slit2*. **j**, *Tbx5*$^{del/+}$;*Ntn1*$^{+/-}$ compound heterozygous embryos displayed a decrease of membranous VSDs (log OR -5.3; p=1x10^{-3} by a Generalized Linear Model without adjustments for multiple comparisons), relative to the expected incidence of membranous

1109 VSDs if there was no genetic interaction between *Tbx5* and *Ntn1,* but not changes to prevalence
1110 of muscular VSDs (log OR 0.12; p=0.93). **k-v**, Machine-learning based quantitative morphometry
1111 of metrics for (k-p) *Tbx5*$^{del/+}$ and *Ntn1*$^{+/-}$ or (q-v) *Tbx5*$^{del/+}$ and *Slit2*$^{+/-}$ by genotype. IVS,
1112 interventricular septum. Significance determined by two-sided Fisher's exact test (*p<0.05,
1113 **p<0.01, ***p<0.001). (k) **p=0.0059, (l)*p=0.0337, (m) *p=0.0196, (q)***p=0.0008, *p=0.0468.
1114 All scale bars are 200 microns.
1115
1116
1117

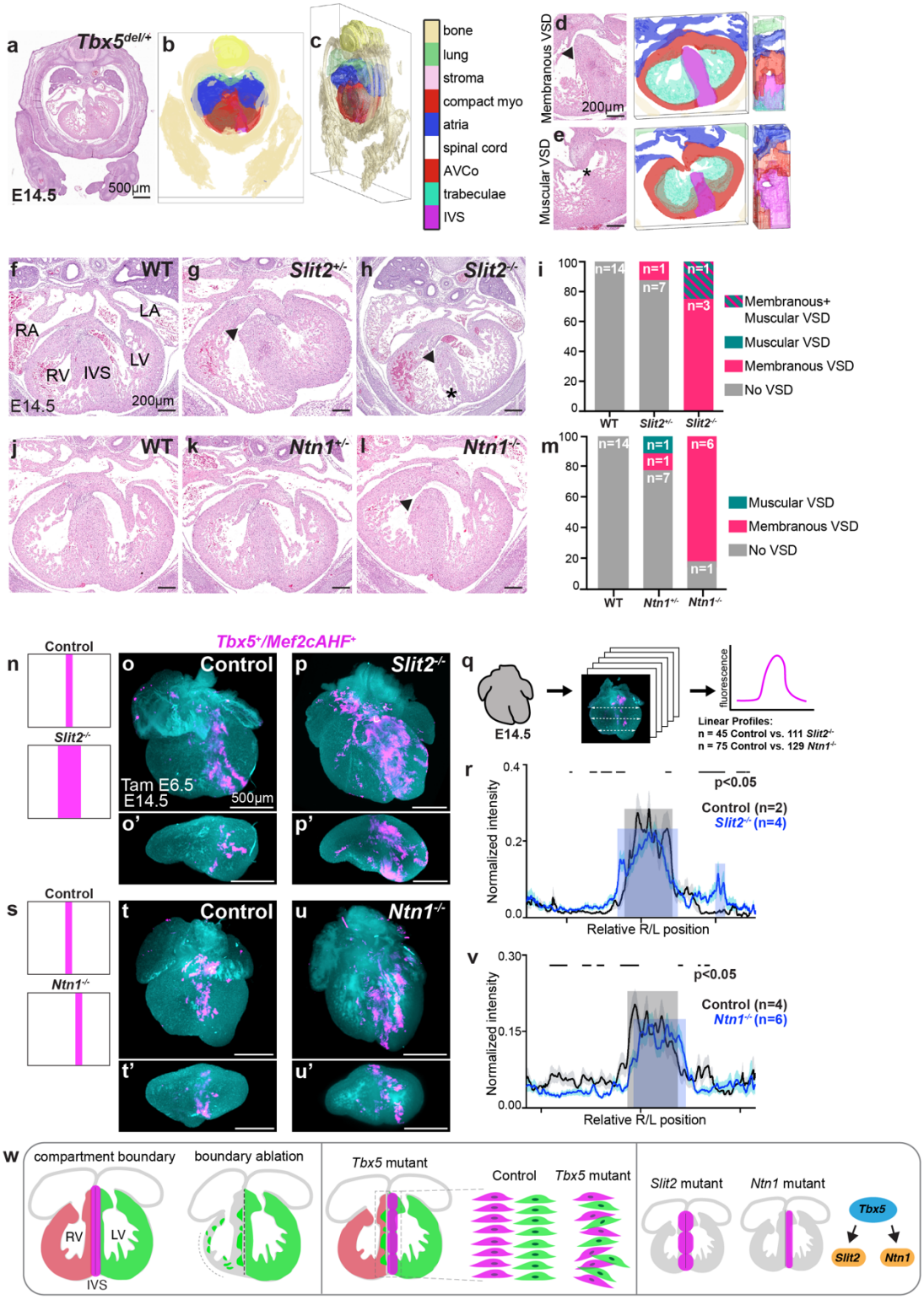

Figure 6. *Slit2* and *Ntn1* are essential for proper ventricular septation and compartment boundary regulation. a-e, Machine learning-based 3-D reconstructions of the embryonic heart and other tissues from histology at E14.5 were used for quantitative morphometric analysis of the embryonic heart (Extended Data Fig. 9, Extended Data Fig. 10). Compact myo, compact

myocardium; AVCo, atrioventricular complex region; IVS, interventricular septum. **d, e**, A 3-D reconstruction of a membranous ventricular septal defect (VSD) anteriorly and muscular VSD posteriorly from a *Tbx5*$^{del/+}$ mutant heart. **f-h**, Histology and (**i**) incidence of muscular or membranous (arrowhead) ventricular septal defects (VSDs) of *Slit2* mutants are shown. Membranous VSDs were enriched in *Slit2*$^{-/-}$ (n=3/4, log OR 5.0, p=0.02 by a Generalized Linear Model without adjustments for multiple comparisons) and *Slit2*$^{+/-}$ (n=1/8, OR 2.5, p=0.02). Asterisk demarcates non-compacted interventricular septum (IVS). **j-l**, Histology and (**m**) incidence of muscular or membranous ventricular septal defects (VSDs) of *Ntn1* mutants are shown. Membranous VSDs were enriched in in *Ntn1*$^{-/-}$ (n=6/7, log OR 6.32, p=0.0052 by a Generalized Linear Model without adjustments for multiple comparisons) and *Ntn1*$^{+/-}$ (n=1/9, OR 3.17, p=0.0052 by a Generalized Linear Model without adjustments for multiple comparisons). **n-r**, Lightsheet imaging of *Slit2*$^{-/-}$ mutant (*Tbx5*$^{CreERT2/+}$;*Mef2cAHF-DreERT2*;*ROSA26*$^{Ai66/+}$;*Slit2*$^{-/-}$)(n=4) hearts at E14.5 showed a broadened distribution of the *Tbx5*$^{+}$/*Mef2cAHF*$^{+}$ lineage (tdTomato^{+} immunostaining) compared to controls (*Tbx5*$^{CreERT2/+}$;*Mef2cAHF-DreERT2*;*ROSA26*$^{Ai66/+}$;*Slit2*$^{+/+}$)(n=2), as (**r**) quantified by linear profiles of fluorescence signals. Gray shading represents control signal, and periwinkle represents mutant signal. Significance of $p<0.05$ was determined by Welch's two-sided t-test at each position along the right-left axis. **s-v**, Lightsheet imaging of *Ntn1*$^{-/-}$ mutant (*Tbx5*$^{CreERT2/+}$;*Mef2cAHF-DreERT2*;*ROSA26*$^{Ai66/+}$;*Ntn1*$^{-/-}$)(n=6) hearts at E14.5 showed a leftward shift in positioning of the *Tbx5*$^{+}$/*Mef2cAHF*$^{+}$ lineage compared to controls (*Tbx5*$^{CreERT2/+}$;*Mef2cAHF-DreERT2*;*ROSA26*$^{Ai66/+}$;*Ntn1*$^{+/+}$)(n=4), as (**v**) quantified by linear profiles. Significance of $p<0.05$ was determined by Welch's two-sided t-test at each position along the right-left axis. Precise p-values are available in Source data. **n, s**, Cartoon depictions. (o', p', t', u') are optical sections that are orthogonal views to (o, p, t, u). **q**, For each sample, three linear profiles (basal, middle, apical) spanned the ventricular chambers from right to left from optical sections every 50 um from anterior to posterior of the heart. Precise values of statistics for (r) and (v) can be found in Source data. **w**, Cartoon depicts summary of findings. All scale bars are 200 microns.

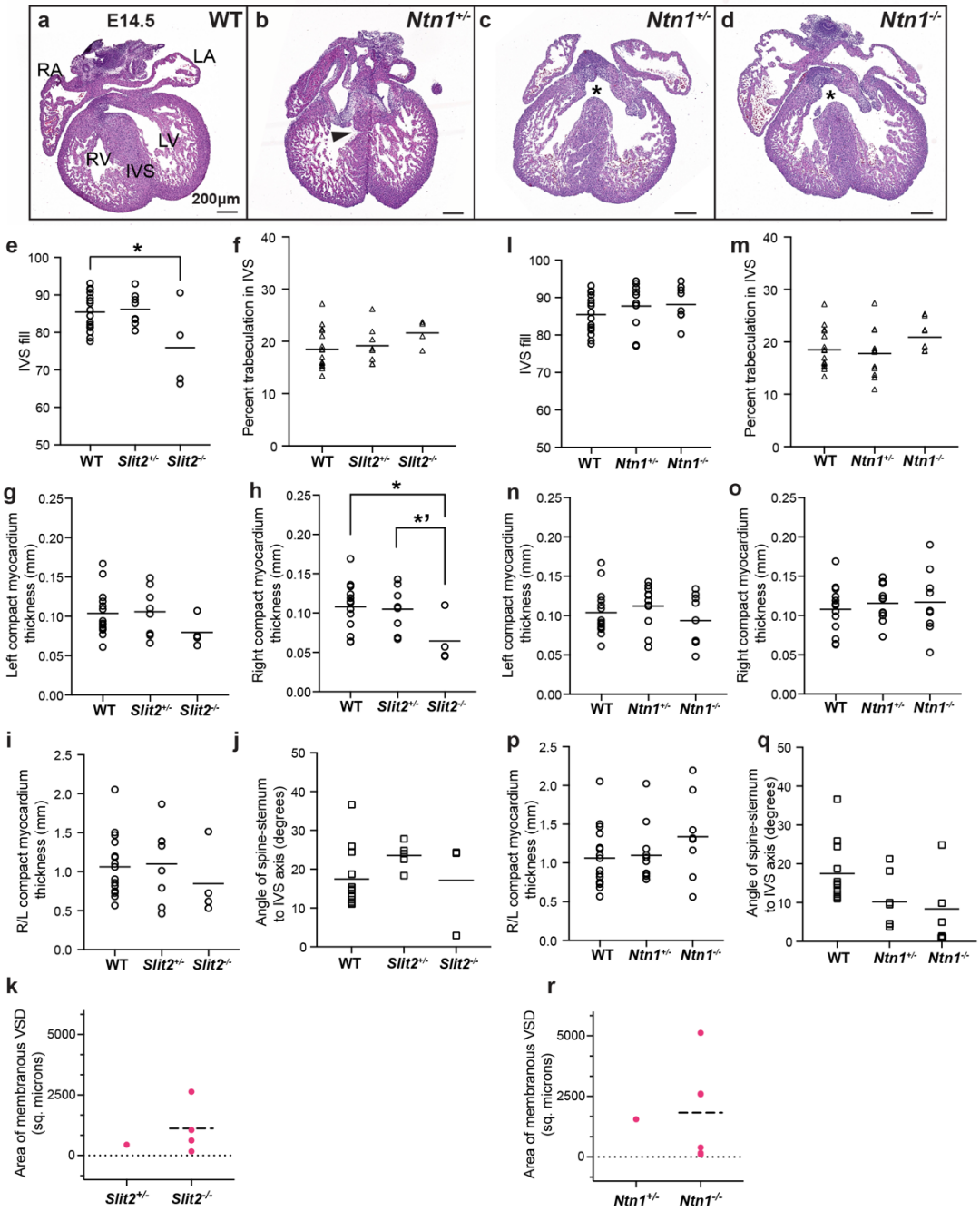

Extended Data Figure 10. Quantitative morphometry of *Slit2* and *Ntn1* mutant hearts. a-d, Additional histology by *Ntn1* genotype at E14.5. Arrowhead, muscular ventricular septal defect (VSD). Asterisk, membranous VSD. Scale bars are 200 microns. **e-p**, Machine learning-based quantitative cardiac morphometrics for (e-k) *Slit2* or (l-r) *Ntn1* mutants. Significance determined by two-sided Fisher's exact test (*p<0.05). **q, r**, Morphometry of the area of membranous VSDs by *Slit2* or *Ntn1* genotypes. (E) *p=0.0184, (H) *p=0.0216, *'p=0.0492.

1160 **References.**
1161

1162 1. Kirby, R. S. The prevalence of selected major birth defects in the United States. *Semin.*
1163 *Perinatol.* **41**, 338–344 (2017).

1164 2. Linde, D. van der *et al.* Birth Prevalence of Congenital Heart Disease Worldwide A
1165 Systematic Review and Meta-Analysis. *J. Am. Coll. Cardiol.* **58**, 2241–2247 (2011).

1166 3. Liu, Y. *et al.* Global birth prevalence of congenital heart defects 1970–2017: updated
1167 systematic review and meta-analysis of 260 studies. *Int. J. Epidemiology* **48**, 455–463 (2019).

1168 4. Cohen, M. S. & Spray, T. L. Surgical management of unbalanced atrioventricular canal
1169 defect. *Semin. Thorac. Cardiovasc. Surg.: Pediatr. Card. Surg. Annu.* **8**, 135–144 (2005).

1170 5. Cruz, M. V. de la, Castillo, M. M., G., L. V., Valencia, A. & Moreno-Rodriguez, R. A. Primitive
1171 interventricular septum, its primordium, and its contribution in the definitive interventricular
1172 septum: In vivo labelling study in the chick embryo heart. *Anatomical Rec* **247**, 512–520 (1997).

1173 6. Harh, J. Y. & Paul, M. H. Experimental cardiac morphogenesis: I. Development of the
1174 ventricular septum in the chick. *Development* **33**, 13–28 (1975).

1175 7. Ben-Shachar, G., Arcilla, R. A., Lucas, R. V. & Manasek, F. J. Ventricular trabeculations in
1176 the chick embryo heart and their contribution to ventricular and muscular septal development.
1177 *Circ. Res.* **57**, 759–766 (1985).

1178 8. Contreras-Ramos, A., Sánchez-Gómez, C., García-Romero, H. L. & Cimarosti, L. O. Normal
1179 Development of the Muscular Region of the Interventricular Septum – I. The Significance of the
1180 Ventricular Trabeculations. *Anat., Histol., Embryol.* **37**, 344–351 (2008).

1181 9. Wessels, A. *et al.* Spatial distribution of “tissue-specific” antigens in the developing human
1182 heart and skeletal muscle. I. An immunohistochemical analysis of creatine kinase isoenzyme
1183 expression patterns. *Anatomical Rec* **228**, 163–176 (1990).

1184 10. Wessels, A. *et al.* The Development of the Atrioventricular Junction in the Human Heart.
1185 *Circ Res* **78**, 110–117 (1996).

1186 11. Lamers, W. H. *et al.* New findings concerning ventricular septation in the human heart.
1187 Implications for maldevelopment. *Circulation* **86**, 1194–1205 (2018).

1188 12. Meilhac, S. M., Esner, M., Kerszberg, M., Moss, J. E. & Buckingham, M. E. Oriented clonal
1189 cell growth in the developing mouse myocardium underlies cardiac morphogenesis. *Journal of*
1190 *Cell Biology* **164**, 97–109 (2004).

1191 13. Koshiba-Takeuchi, K. *et al.* Reptilian heart development and the molecular basis of cardiac
1192 chamber evolution. *Nature* **461**, 95–98 (2009).

1193 14. Christoffels, V. M., Keijser, A. G. M., Houweling, A. C., Clout, D. E. W. & Moorman, A. F. M.
1194 Patterning the Embryonic Heart: Identification of Five Mouse Iroquois Homeobox Genes in the
1195 Developing Heart. *Dev Biol* **224**, 263–274 (2000).

1196 15. Stadtfeld, M., Ye, M. & Graf, T. Identification of interventricular septum precursor cells in the
1197 mouse embryo. *Dev. Biol.* **302**, 195–207 (2007).

1198 16. Cruz, M. V. de la, Sánchez-Gómez, C. & Palomino, M. A. The primitive cardiac regions in
1199 the straight tube heart (Stage 9) and their anatomical expression in the mature heart: An
1200 experimental study in the chick embryo. *J. Anat.* **165**, 121–31 (1989).

1201 17. Moorman, A., Webb, S., Brown, N. A., Lamers, W. & Anderson, R. H. Development of the
1202 heart:(1) formation of the cardiac chambers and arterial trunks. *Heart* **89**, 806–814 (2003).

1203 18. Laura, V. G. *et al.* Incorporation of the first and second heart fields and prospective fate of
1204 the straight heart tube via in vivo labeling of chicken embryos. *PLoS ONE* **15**, e0234069-17
1205 (2020).

1206 19. Franco, D., Kelly, R., Lamers, W. H., Buckingham, M. & Moorman, A. F. M. Regionalized
1207 Transcriptional Domains of Myosin Light Chain 3f Transgenes in the Embryonic Mouse Heart:
1208 Morphogenetic Implications. *Dev Biol* **188**, 17–33 (1997).

1209 20. Cai, C.-L. *et al.* Isl1 identifies a cardiac progenitor population that proliferates prior to
1210 differentiation and contributes a majority of cells to the heart. *Dev Cell* **5**, 877–889 (2003).

1211 21. Meilhac, S. M., Esner, M., Kelly, R. G., Nicolas, J.-F. & Buckingham, M. E. The clonal origin
1212 of myocardial cells in different regions of the embryonic mouse heart. *Dev Cell* **6**, 685–698
1213 (2004).

1214 22. Liang, X. *et al.* HCN4 Dynamically Marks the First Heart Field and Conduction System
1215 Precursors. *Circ Res* **113**, 399–407 (2013).

1216 23. Später, D. *et al.* A HCN4+ cardiomyogenic progenitor derived from the first heart field and
1217 human pluripotent stem cells. *Nat Cell Biol* **15**, 1–10 (2013).

1218 24. Lescroart, F. *et al.* Early lineage restriction in temporally distinct populations of Mesp1
1219 progenitors during mammalian heart development. *Nat Cell Biol* **16**, 829–840 (2014).

1220 25. Devine, W. P., Wythe, J. D., George, M., Koshiba-Takeuchi, K. & Bruneau, B. G. Early
1221 patterning and specification of cardiac progenitors in gastrulating mesoderm. *eLife* **3**, 508
1222 (2014).

1223 26. Lescroart, F. *et al.* Defining the earliest step of cardiovascular lineage segregation by single-
1224 cell RNA-seq. *Science* **359**, 1177–1181 (2018).

1225 27. Kiecker, C. & Lumsden, A. Compartments and their boundaries in vertebrate brain
1226 development. *Nat Rev Neurosci* **6**, 553–564 (2005).

1227 28. Dahmann, C., Basler, K., Dahmann, C. & Basler, K. Compartment boundaries: at the edge
1228 of development. *Trends Genet* **15**, 320–326 (1999).

1229 29. Wang, J. & Dahmann, C. Establishing compartment boundaries in Drosophila wing imaginal
1230 discs: An interplay between selector genes, signaling pathways and cell mechanics. *Semin Cell*
1231 *Dev Biol* **107**, 161–169 (2020).

1232 30. Kimmel, R. A. *et al.* Two lineage boundaries coordinate vertebrate apical ectodermal ridge
1233 formation. *Genes Dev.* **14**, 1377–1389 (2000).

1234 31. Arques, C. G., Doohan, R., Sharpe, J. & Torres, M. Cell tracing reveals a dorsoventral
1235 lineage restriction plane in the mouse limb bud mesenchyme. *Development* **134**, 3713–3722
1236 (2007).

1237 32. Qiu, Q., Chen, H. & Johnson, R. L. Lmx1b-expressing cells in the mouse limb bud define a
1238 dorsal mesenchymal lineage compartment. *Genesis* **47**, 224–233 (2009).

1239 33. Zervas, M., Millet, S., Ahn, S. & Joyner, A. L. Cell Behaviors and Genetic Lineages of the
1240 Mesencephalon and Rhombomere 1. *Neuron* **43**, 345–357 (2004).

1241 34. Franco, D. *et al.* Left and right ventricular contributions to the formation of the
1242 interventricular septum in the mouse heart. *Dev Biol* **294**, 366–375 (2006).

1243 35. Madisen, L. *et al.* Transgenic Mice for Intersectional Targeting of Neural Sensors and
1244 Effectors with High Specificity and Performance. *Neuron* **85**, 942–958 (2015).

1245 36. Maxwell, F., Maxwell, I. H. & Glode, L. M. Cloning, sequence determination, and expression
1246 in transfected cells of the coding sequence for the tox 176 attenuated diphtheria toxin A chain.
1247 *Mol Cell Biol* **7**, 1576–1579 (2007).

1248 37. Wu, S., Wu, Y. & Capecchi, M. R. Motoneurons and oligodendrocytes are sequentially
1249 generated from neural stem cells but do not appear to share common lineage-restricted
1250 progenitors in vivo. *Development* **133**, 581–590 (2006).

1251 38. Erhardt, V. *et al.* Systematic optimization and prediction of cre recombinase for precise
1252 genome editing in mice. *Genome Biol.* **26**, 85 (2025).

1253 39. Bao, J., Ma, H., Schuster, A., Lin, Y. & Yan, W. Incomplete cre-mediated excision leads to
1254 phenotypic differences between Stra8-iCre; Mov10l1lox/lox and Stra8-iCre; Mov10l1lox/Δ mice.
1255 *genesis* **51**, 481–490 (2013).

1256 40. Haldar, M., Karan, G., Tvrdik, P. & Capecchi, M. R. Two Cell Lineages, myf5 and myf5-
1257 Independent, Participate in Mouse Skeletal Myogenesis. *Dev. Cell* **14**, 437–445 (2008).

1258 41. Vincentz, J. W., Toolan, K. P., Zhang, W. & Firulli, A. B. Hand factor ablation causes
1259 defective left ventricular chamber development and compromised adult cardiac function. *Plos*
1260 *Genet* **13**, e1006922 (2017).

1261 42. Basson, C. T. *et al.* Mutations in human TBX5 [corrected] cause limb and cardiac
1262 malformation in Holt-Oram syndrome. *Nat Genet* **15**, 30–35 (1997).

1263 43. Li, Q. Y. *et al.* Holt-Oram syndrome is caused by mutations in TBX5, a member of the
1264 Brachyury (T) gene family. *Nat Genet* **15**, 21–29 (1997).

1265 44. Kathiriya, I. S. *et al.* Modeling Human TBX5 Haploinsufficiency Predicts Regulatory
1266 Networks for Congenital Heart Disease. *Dev Cell* **56**, 292-309.e9 (2021).

1267 45. Bruneau, B. G. *et al.* A Murine Model of Holt-Oram Syndrome Defines Roles of the T-Box
1268 Transcription Factor Tbx5 in Cardiogenesis and Disease. *Cell* **106**, 709–721 (2001).

1269 46. Verzi, M. P., McCulley, D. J., Val, S. D., Dodou, E. & Black, B. L. The right ventricle, outflow
1270 tract, and ventricular septum comprise a restricted expression domain within the
1271 secondary/anterior heart field. *Dev Biol* **287**, 134–145 (2005).

1272 47. Mori, A. D. & Bruneau, B. G. TBX5 mutations and congenital heart disease: Holt-Oram
1273 syndrome revealed. *Curr Opin Cardiol* **19**, 211–215 (2004).

1274 48. Larrieu-Lahargue, F., Thomas, K. R. & Li, D. Y. Netrin Ligands and Receptors: Lessons
1275 From Neurons to the Endothelium. *Trends Cardiovas Med* **22**, 44–47 (2012).

1276 49. Mommersteeg, M. T. M., Yeh, M. L., Parnavelas, J. G. & Andrews, W. D. Disrupted Slit-
1277 Robo signalling results in membranous ventricular septum defects and bicuspid aortic valves.
1278 *Cardiovasc Res* **106**, 55–66 (2015).

1279 50. Agustin, J. T. S. *et al.* Genetic link between renal birth defects and congenital heart disease.
1280 *Nat Commun* **7**, 11103–11 (2016).

1281 51. Kruszka, P. *et al.* Loss of function in ROBO1 is associated with tetralogy of Fallot and septal
1282 defects. *J Med Genet* **54**, 825 (2017).

1283 52. Fotiou, E. *et al.* Integration of Large-Scale Genomic Data Sources With Evolutionary History
1284 Reveals Novel Genetic Loci for Congenital Heart Disease. *Circ.: Genom. Precis. Med.* **12**, 442–
1285 451 (2019).

1286 53. Opitz, R. *et al.* Functional Zebrafish Studies Based on Human Genotyping Point to Netrin-1
1287 as a Link Between Aberrant Cardiovascular Development and Thyroid Dysgenesis.
1288 *Endocrinology* **156**, 377–388 (2015).

1289 54. Li, Y. *et al.* Global genetic analysis in mice unveils central role for cilia in congenital heart
1290 disease. *Nature* **521**, 1–16 (2015).

1291 55. Akerberg, B. N. *et al.* A reference map of murine cardiac transcription factor chromatin
1292 occupancy identifies dynamic and conserved enhancers. *Nat Commun* **10**, 4907 (2019).

1293 56. Bin, J. M. *et al.* Complete Loss of Netrin-1 Results in Embryonic Lethality and Severe Axon
1294 Guidance Defects without Increased Neural Cell Death. *Cell Reports* **12**, 1099–1106 (2015).

1295 57. Lewandoski, M., Meyers, E. N. & Martin, G. R. Analysis of Fgf8 gene function in vertebrate
1296 development. *Cold Spring Harb Sym* **62**, 159–68 (1997).

1297 58. Kiemen, A. L. *et al.* CODA: quantitative 3D reconstruction of large tissues at cellular
1298 resolution. *Nat Methods* 1–10 (2022) doi:10.1038/s41592-022-01650-9.

1299 59. Vincent, J. P. Compartment boundaries: where, why and how? *Int. J. Dev. Biol.* **42**, 311–5
1300 (1998).

1301 60. Lawrence, P. A. & Struhl, G. Morphogens, compartments, and pattern: lessons from
1302 drosophila? *Cell* **85**, 951–961 (1996).

1303 61. Matos-Nieves, A. *et al.* Expression of Netrin-1 in the developing mouse heart. *Gene Expr.*
1304 *Patterns* 119398 (2025) doi:10.1016/j.gep.2025.119398.

1305 62. Barlow, G. M. *et al.* Down syndrome congenital heart disease: A narrowed region and a
1306 candidate gene. *Genet. Med.* **3**, 91–101 (2001).

1307 63. Jin, S. C. *et al.* Contribution of rare inherited and de novo variants in 2,871 congenital heart
1308 disease probands. *Nat Genet* **49**, 1593–1601 (2017).

1309 64. Dong, W. *et al.* Recessive genetic contribution to congenital heart disease in 5,424
1310 probands. *Proc. Natl. Acad. Sci.* **122**, e2419992122 (2025).

1311 65. Lu, X. *et al.* The netrin receptor UNC5B mediates guidance events controlling
1312 morphogenesis of the vascular system. *Nature* **432**, 179–186 (2004).

1313 66. Navankasattusas, S. *et al.* The netrin receptor UNC5B promotes angiogenesis in specific
1314 vascular beds. *Development* **135**, 659–667 (2008).

1315 67. VanDusen, N. J. *et al.* Hand2 Is an Essential Regulator for Two Notch-Dependent Functions
1316 within the Embryonic Endocardium. *Cell Rep.* **9**, 2071–2083 (2014).

1317 68. George, R. M. *et al.* Single cell evaluation of endocardial HAND2 gene regulatory networks
1318 reveals critical HAND2 dependent pathways impacting cardiac morphogenesis. *Development*
1319 **150**, (2023).

1320 69. Tasic, B. *et al.* Site-specific integrase-mediated transgenesis in mice via pronuclear
1321 injection. *Proc National Acad Sci* **108**, 7902–7907 (2011).

1322 70. Madisen, L. *et al.* A robust and high-throughput Cre reporting and characterization system
1323 for the whole mouse brain. *Nat Neurosci* **13**, 133–140 (2010).

1324 71. Dominguez, M. H., Krup, A. L., Muncie, J. M. & Bruneau, B. G. Graded mesoderm assembly
1325 governs cell fate and morphogenesis of the early mammalian heart. *Cell* **186**, 479-496.e23
1326 (2023).

1327 72. Schindelin, J. *et al.* Fiji: an open-source platform for biological-image analysis. *Nat. Methods*
1328 **9**, 676–682 (2012).

1329 73. Kirshner, H., Aguet, F., Sage, D. & Unser, M. 3-D PSF fitting for fluorescence microscopy:
1330 implementation and localization application. *J. Microsc.* **249**, 13–25 (2013).

1331 74. Hörl, D. *et al.* BigStitcher: reconstructing high-resolution image datasets of cleared and
1332 expanded samples. *Nat Methods* **16**, 870–874 (2019).

1333 75. Tinevez, J.-Y. *et al.* TrackMate: An open and extensible platform for single-particle tracking.
1334 *Methods* **115**, 80–90 (2017).

1335 76. Satija, R., Farrell, J. A., Gennert, D., Schier, A. F. & Regev, A. Spatial reconstruction of
1336 single-cell gene expression data. *Nat Biotechnol* **33**, 495–502 (2015).

1337 77. Butler, A., Hoffman, P., Smibert, P., Papalexi, E. & Satija, R. Integrating single-cell
1338 transcriptomic data across different conditions, technologies, and species. *Nat Biotechnol* **48**,
1339 1070–17 (2018).

1340 78. Stuart, T. *et al.* Comprehensive Integration of Single-Cell Data. *Cell* **177**, 1–37 (2019).

1341 79. Becht, E. *et al.* Dimensionality reduction for visualizing single-cell data using UMAP. *Nat*
1342 *Biotechnol* (2018) doi:10.1038/nbt.4314.

1343 80. Forjaz, A. *et al.* Three-dimensional assessments are necessary to determine the true,
1344 spatially resolved composition of tissues. *Cell Rep. Methods* **5**, 101075 (2025).

1345
1346
1347
1348